JGR Solid Earth

RESEARCH ARTICLE
10.1029/2018JB015960

Universal and Nonuniversal Aperture-to-Length Scaling of Opening Mode Fractures Developing in a Particle-Based Lattice Solid Model

Franziska Mayrhofer[1], Martin P. J. Schöpfer[1], and Bernhard Grasemann[1]

[1]Department for Geodynamics and Sedimentology, University of Vienna, Vienna, Austria

Key Points:
- A particle-based lattice solid model consistent with linear elastic fracture mechanics is used to model opening mode fracture systems
- Prior to formation of the multiple-segment fracture zone, aperture-to-length scaling is linear
- Aperture-to-length scaling is nonuniversal in fracture systems exhibiting strong segment interactions

Supporting Information:
- Supporting Information S1
- Data Set S1

Correspondence to:
M. P. J. Schöpfer,
martin.schoepfer@univie.ac.at

Citation:
Mayrhofer, F., Schöpfer, M. P. J., & Grasemann, B. (2019). Universal and nonuniversal aperture-to-length scaling of opening mode fractures developing in a particle-based lattice solid model. *Journal of Geophysical Research: Solid Earth*, *124*, 3197–3218. https://doi.org/10.1029/2018JB015960

Received 13 APR 2018
Accepted 5 FEB 2019
Accepted article online 9 FEB 2019
Published online 29 MAR 2019

Abstract Opening-mode fractures, such as joints, veins, and dykes, frequently exhibit power-law aperture-to-length scaling, with scaling exponents typically ranging from 0.5 to 2. However, published high quality outcrop data and continuum-based numerical models indicate that fracture aperture-to-length scaling may be nonuniversal, with scaling being superlinear for short fractures and sublinear for long fractures. Here we revisit these published results by means of a particle-based lattice solid model, which is validated using predictions from linear elasticity and linear elastic fracture mechanics. The triangular lattice model composed of breakable elastic beams, with strengths drawn from a Weibull distribution, is used to investigate the fracture aperture-to-length scaling that emerges in a plate subjected to extension. The modeled fracture system evolution is characterized by two stages which are separated by the strain at which peak-stress occurs. During the pre-peak-stress stage, aperture-to-length scaling is universal with a power-law exponent of about one. Shortly after the material has attained its maximum load bearing capacity, which coincides with the formation of a multiple-segment fracture zone, aperture-to-length scaling becomes nonuniversal, with power-law exponents being consistent with earlier studies. The results presented here confirm that deviation from universal scaling laws is a consequence of fracture interaction. More specifically, the onset of nonuniversal aperture-to-length scaling coincides with the formation of a multiple-segment fracture zone.

1. Introduction

The maximum displacement to length scaling of fractures is typically expressed as $d_{max} = cL^b$ (Bonnet et al., 2001), where L is the fracture length, c the preexponential constant, b the power-law scaling exponent, and in the case of opening mode fractures (e.g., joints and veins), d_{max} is the maximum opening displacement, also referred to as fracture width or aperture. Analytical solutions, based on linear elastic fracture mechanics (LEFM), for an isolated critically stressed crack subjected to a remote tension predict that the maximum opening displacement is proportional to the square root of the crack length (e.g., Olson, 2003; Scholz, 2010)

$$d_{max} = \frac{K_{Ic}(1-\nu^2)}{E\sqrt{\pi/8}}\sqrt{L}, \tag{1}$$

where E is the Young's Modulus, ν the Poisson's ratio, and K_{Ic} the mode I fracture toughness of the material. Hence, maximum opening displacement and associated crack length measurements plotted on $\log d_{max}$ versus $\log L$ graphs are expected to fall onto a line with slope b equal to 0.5 if LEFM conditions apply. Such a scaling law with $b < 1$ is sometimes referred to as sublinear (Olson, 2003).

The existence of such a universal scaling law and the value of the power-law exponent are however highly debated topics (e.g., Olson & Schultz, 2011; Scholz, 2010, 2011; Schultz et al., 2008, 2013). Moreover, high quality outcrop data suggest that aperture-to-length scaling may be nonuniversal, so that at a certain (critical or characteristic) length scale (x^*), a change of the power-law exponent occurs (Figure 1a). On the basis of outcrop data from Icelandic fracture swarms, Hatton et al. (1994) suggest that up to a certain critical crack length, resistance to crack growth is dependent on the local microstructure (in the form of columnar jointing), while above the critical length scale, fracture growth is controlled by the bulk properties of the material. The nonuniversal aperture-to-length scaling proposed for the Icelandic fracture swarms was successfully reproduced by numerical modeling of fracture system growth (Renshaw & Park, 1997; Figure 1b).

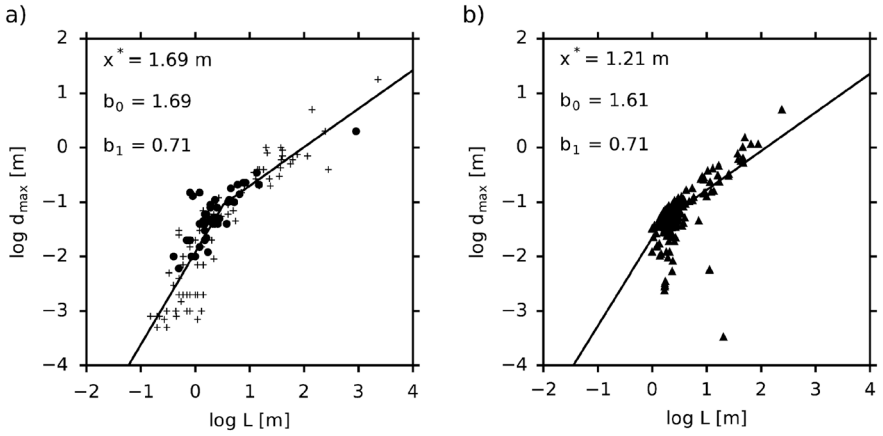

Figure 1. Nonuniversal aperture-to-length scaling of natural and numerically generated fractures plotted on $\log d_{max}$ versus $\log L$ graphs. (a) Data from natural fracture populations at Kelduhverfi (crosses) and Mývatn (dots), Iceland (data from Hatton et al., 1994). (b) Data derived from numerical models in which fractures grow from initially equal-length, parallel flaws randomly distributed in a two-dimensional linear elastic medium subjected to a remote stress boundary condition (data from Renshaw & Park, 1997). Both data sets are fitted using nonlinear least-squares and a bilinear scaling law of the form given in Main et al. (1999; see also equation (9)). The best-fit slope values, b_0 and b_1, and the changepoint, x^*, are given in each graph.

Since these models do not contain any local microstructure with a characteristic length scale, the break in slope that emerged from these numerical models is interpreted as the length at which the apertures of smaller fractures are affected by stress perturbations induced by larger fractures.

The numerical models by Renshaw and Park (1997) consist of initially equal-length, parallel flaws randomly distributed in a two-dimensional linear elastic medium subjected to a remote stress boundary condition. Analytical solutions for isolated cracks are used to solve the interaction between each pair of fractures from which the energy available for each fracture tip, and hence, its propagation distance can be obtained. Analysis of the fracture system developments suggests that mechanical interaction between fractures reduce the energy release rates, so that mechanical interaction within the fracture set restricts, rather than promotes, fracture growth (Renshaw & Pollard, 1994).

Mechanical interaction between the fractures causes and is enhanced by clustering, affecting aperture-to-length scaling as suggested by the field studies of Vermilye and Scholz (1995), who demonstrated that single-segmented fractures follow a linear trend, whereas multiple-segmented fractures show greater scatter and are marginally better fitted by a square-root function; individual segments comprising multiple-segment fractures exhibit d_{max}/L values greater than those of single-segment fractures. The numerical spring models of Walmann et al. (1996) furthermore suggest that the power-law exponent may depend on the amount of extension. Derivations from idealized power-law scaling laws are hence the result of mechanical fracture interaction and fracture segmentation (Olson, 2003; Pollard et al., 1982), and the degree of fracture clustering is thought to be a result of the propagation velocity distribution controlled by the subcritical index (Olson, 2004).

Many of the above observations are derived from numerical models, which are either based on continuum mechanics (e.g., boundary elements; Olson, 2004) so that fractures grow from preexisting flaws (their initial density may be varied; e.g., Renshaw & Pollard, 1994) or are composed of a network of nodes connected by springs (Spyropoulos et al., 2002; Walmann et al., 1996) where fractures grow by the progressive breakage of springs (which in regular lattices typically have breakage threshold values taken from a probability density function; e.g., Hooker & Katz, 2015). In the present study an alternative method for simulating fracture system growth, namely, a simplified two-dimensional Distinct Element Method (DEM) approach, is used. In contrast to the widely used mass-spring-damper models used to date, the springs connecting the masses (circular particles in the DEM) have a finite width and can resist relative rotation so that not only a force but also a moment develops. Fracture systems are generated in a two-dimensional lattice with heterogeneous strength under quasi-static conditions with monotonically increasing boundary displacements, rather than under constant remote stress conditions as often used in continuum mechanics based approaches.

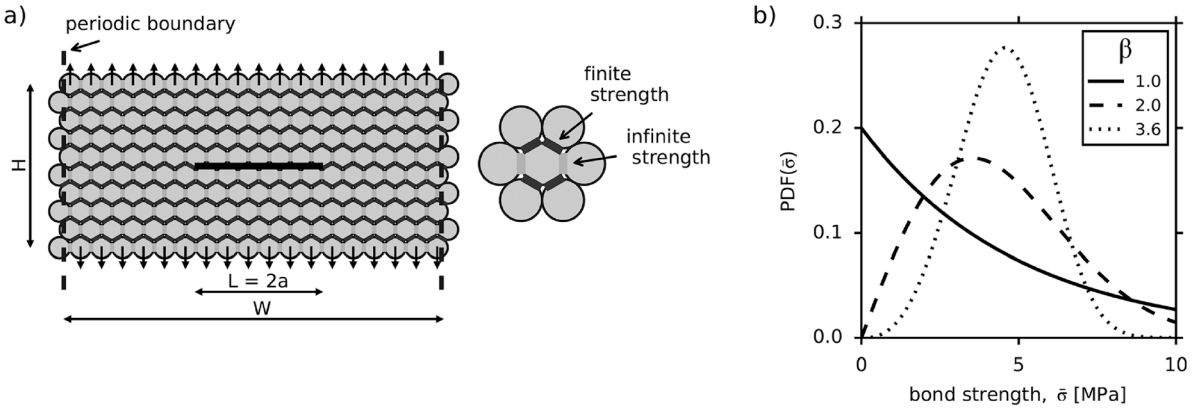

Figure 2. (a) The particle-based lattice solid model composed of equisized particles (discs) bonded at their contacts. Light gray bonds are unbreakable, whereas dark gray bonds can break (inset shows bonds between one particle and its neighbors). For clarity, the bonds are plotted with half of their actual width. Dashed lines show the positions of the periodic boundaries. Arrows point in the direction of the applied velocity. The horizontal model dimension is the width W, and the bold line represents a periodic, colinear fracture of length $L = 2a$, along which bonds are removed prior to extension. The initial model height H is the distance between the particle centers comprising the top and bottom rows. (b) Probability density function of a two-parameter Weibull distribution (equation (2)) for scale parameter $\alpha = 5$ MPa and varying shape parameters β. Bond strengths are drawn from these distributions via equation (3) in the fracture system models (section 3.3).

The results presented here illustrate that LEFM behavior emerges from simple beam breakage laws and confirm that deviation from universal scaling laws are a consequence of fracture interaction. More specifically, the onset of nonuniversal aperture-to-length scaling coincides with the formation of a multiple-segment fracture zone.

2. Methods

2.1. The Particle-Based Lattice Solid Model

Numerical simulations are performed with the commercially available DEM software Particle Flow Code in two dimensions (Itasca Consulting Group, Inc, 2008), which is widely used to numerically solve problems in geomechanics. The DEM is a procedure that allows finite displacement and rotations of discrete bodies (particles). Particle movement, caused by externally applied forces and body forces and particle interaction, is treated as a dynamic process, with states of equilibrium developing whenever the internal forces balance (Cundall, 1988; Hart et al., 1988). Typically, the discontinuum is represented by a dense packing of nonuniform-sized circular rigid particles, which occupy a finite amount of space and have a finite mass. The rigid particles can only interact via their soft contacts, which possess normal and shear stiffness and optional strength parameters (e.g., friction). Particles may also be bonded at contacts (bonded particle model [BPM]); these bonds carry load and break if their strength is exceeded. A detailed description of the DEM and the BPM approach is provided in Potyondy and Cundall (2004).

Here a simplified BPM approach is used. The circular, equisized particles (diameter $d = 1$ m) are packed regularly to form a triangular (hexagonal) lattice (Figure 2a), which, as shown later, behaves as an isotropic linear elastic solid. The principal reason for using a triangular rather than a square lattice is that the former is elastically isotropic and the latter orthotropic (this is strictly speaking just the case when only the nearest neighbors are bonded; a square lattice becomes isotropic when neighbors are additionally bonded diagonally; Monette & Anderson, 1994). In an earlier study, we have run a similar suite of models with a square lattice which yielded, in terms of aperture-to-length scaling (section 3.3), very similar results (Mayrhofer et al., 2014). However, the square lattice could not reproduce theoretical displacement profiles derived from linear elasticity (section 3.1) so that the square lattice approach, which at the particle-scale provides planar cracks, was discarded. In the triangular lattice, fractures are hence, at the particle scale, "jagged," which under pure opening poses however no problem; the jaggedness results in shear displacements which, if a fracture closes, would result in shear tractions at frictional contacts, which is however avoided in the present study by setting the post-failure contact friction coefficient to zero (Table 1).

Table 1
Properties of Lattice Model

Symbol	Description[a]	Value
Particle properties		
R	Particle radius	0.5 m
ρ_p	Particle density[b]	1,000 kg/m^3
Pre-failure contact properties		
$\bar{E}_c$	Bond Young's modulus	14 GPa
$\bar{\kappa}$	Bond stiffness ratio	2.5
$\bar{\lambda}$	Bond width multiplier	1.0
$\bar{\sigma}_c$	Bond tensile strength[c]	5 MPa
$\bar{\tau}_c$	Bond shear strength	∞
E_c	Contact Young's modulus[d]	0.0
Post-failure contact properties		
E_c	Contact Young's modulus[d]	14 GPa
μ_c	Contact friction coefficient	0.0
Bulk properties		
E	Young's modulus (equation (A2))	19.52 GPa
ν	Poisson's ratio (equation (A2))	0.15
T	Tensile strength (equation (A4))	9.815 MPa
K_{Ic}	Mode I fracture toughness (for $R \ll W$)	~10 MPa m$^{0.5}$

[a]A full definition of particle/bond properties is given by Potyondy and Cundall (2004). [b]Particles must have a finite mass for the computation of a time step. In quasi-static systems without gravitational acceleration, the actual particle mass does not effect the model outcome. [c]In the fracture system models, bonds have random strength values drawn from a Weibull distribution (equation (2)) with scale parameter $\alpha = \bar{\sigma}_c$. [d]Setting the contact modulus to zero ensures that the entire contact force is carried by the bonds. After bond breakage, a finite contact modulus is assigned so that the "fracture walls" have a stiffness.

Particles are bonded together with so-called parallel bonds, which, prior to failure, carry the entire contact load. Bond failure occurs when the maximum tensile/shear stress acting on the parallel bond periphery, which is calculated from beam theory using relative velocities and rotation between bonded particles (Potyondy & Cundall, 2004), exceeds the predefined bond's tensile/shear strength; fracture propagation within the lattice hence does not require the computation of near crack-tip stress intensity factors. Although schemes exist for implementing stress corrosion permitting the modeling of subcritical crack growth (e.g., Potyondy, 2007), such a time-dependent behavior via a damage-rate law in the bond formulation is, for simplicity's sake, not implemented in the present study but could be an interesting avenue for future research. A linear contact model is assigned to contacts after bond breakage has occurred, so that the fracture walls have a finite stiffness in case of fracture closure. Bonds normal to the extension direction have infinite strengt h and cannot break (light gray in Figure 2a). Strength heterogeneity is introduced by selecting bond strength values randomly from Weilbull distributions (Figure 2b). This model setup results in stacked parallel unbreakable linear elastic beams which are glued together with finite strength cement, where, in the present context, the breakage of cement corresponds to fractures in rock. The advantage of this approach is that model generation and analysis is greatly simplified. The disadvantage is that fractures developing between one pair of particle rows cannot link with adjacent fractures, so that only tip-to-tip linkage of colinear fractures is possible. In that respect, our models are comparable to the models by Olson (2004) or Renshaw and Pollard (1994). Importantly, it has been shown by others that "soft linkage" gives a very similar opening distribution to actual linkage in en échelon arrays, but the details are dependent on the amount of fracture overlap relative to their separation (e.g., Olson, 2003; Pollard et al., 1982).

In order to avoid boundary effects (the stress intensity factor of an edge crack is greater than of an internal crack; Tada et al., 2000), periodic boundaries are used so that the medium is effectively infinite normal to the extension direction (Figure 2a). Forces, moments, and displacements of the outermost particles on the

right side are assigned to the particles on the left side of the model. This means that if a fracture propagates through a periodic boundary, it will automatically reappear on the other side of the model. Extension of this "plate" is achieved by applying outward directed velocities to the bottom and top particle rows (Figure 2a). The boundary velocity is low enough to ensure quasi-static conditions throughout the model run, so that at any point, during the model run, the fracture configuration is stable, implying that a sudden halt of the boundary displacement would not result in further fracture propagation or opening.

The bulk properties of the lattice model, such as elastic constants, tensile strength, and mode I fracture toughness, are described in detail in Appendix A. The particle/contact properties used in the present study and the resulting bulk properties are summarized in Table 1.

2.2. Selection of Model Properties

Using the relations given in Appendix A, contact properties (stiffness and strength) were selected in order to mimic the behavior of brittle rock with a plane strain Young's modulus of 20 GPa, a Poisson's ratio of 0.15, and a tensile strength of 10 MPa, resulting in a mode I fracture toughness of ~10 MPa $m^{0.5}$ (as summarized in Table 1). Note that bond stiffness and bond strength are contact properties, whereas fracture toughness, for example, is an emergent property. The elastic properties were not varied in any of the models presented here, but different bond strength values and distributions were used resulting in heterogeneous fracture toughness. Fully elastic behavior (section 3.2) is achieved by setting the bond strength to infinity. Constant finite bond strength values, resulting in constant fracture toughness, were used for comparing lattice model results with LEFM predictions (section 3.1). For the fracture system models (section 3.3), strength heterogeneity is introduced by random variation of the bond strength using a two-parameter Weibull distribution (e.g., as in the models of Hooker & Katz, 2015). The probability density function *We* of a Weibull random variable $x \geq 0$ is

$$We(x) = \frac{\beta}{\alpha}\left(\frac{x}{\alpha}\right)^{\beta-1} \exp\left(-\left(\frac{x}{\alpha}\right)^{\beta}\right). \tag{2}$$

The Weibull distribution is a continuous probability distribution, which only returns positive values and has two dimensionless input parameters, the scale parameter α and the shape parameter β. The parameter α changes the scale along the x axis (bond strength in the present study), whereas the parameter β determines the function's shape. Certain values of β provide other well-known distributions: If $\beta = 1$, the Weibull distribution is identical to the exponential distribution; if $\beta = 2$, the Weibull distribution is identical to the Rayleigh distribution; and if $\beta = 3.6$, the Weibull distribution approximates the normal distribution (Figure 2b).

Tensile bond strength values ($\bar{\sigma}_c$) with a Weibull distribution are achieved using random values X drawn from a uniform size distribution between 0 and 1:

$$\bar{\sigma}_c = \alpha[-\log(X)]^{\frac{1}{\beta}} \qquad X \sim U([0,1]). \tag{3}$$

In the present study the fracture system models were run using a constant scale parameter α equal to the bond strength used in the homogeneous models and β values equal to 1, 2, and 3.6, so that "strength heterogeneity" increases with decreasing β value.

3. Results and Discussion

In this section the main results of the present study are presented. First, we present the scaling for critically stressed, collinear, periodic fractures and illustrate that LEFM behavior emerges from our lattice model (section 3.1). Then we illustrate the aperture-length scaling of parallel, randomly positioned nonpropagating fractures (section 3.2). Finally, we present model results of fracture system development in materials with heterogeneous strength, subjected to constant boundary displacement conditions, and show the effects of the degree of strength heterogeneity and strain on aperture-to-length scaling (section 3.3).

3.1. Scaling of Collinear, Periodic Cracks at Incipient Propagation

The purpose of the models presented in this subsection is twofold: First, they illustrate that displacement profiles derived from linear elasticity can be reproduced with our lattice model. Second, they show that the aperture-to-length scaling predicted for critically stressed cracks emerges from these models.

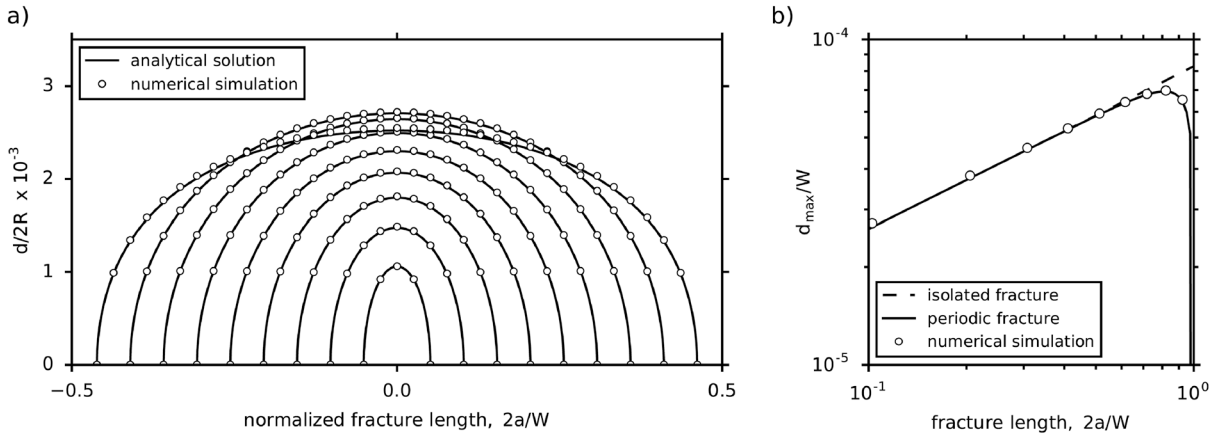

Figure 3. Scaling of collinear, periodic cracks at incipient failure. (a) Displacement profiles extracted from lattice models (white dots) and comparison with analytical solution (equation (4)). (b) Log-log plot of maximum normalized aperture $d_{max}/2R$ versus fracture length $2a$, normalized by crack spacing W. Model results (white dots) are compared with analytical solutions for isolated cracks (dashed line; equation (1)) and collinear, periodic cracks (solid curve; equation (6)) using the bulk properties listed in Table 1.

Tada et al. (2000) provide stress and displacement solutions for a wide range of crack geometries and loading configurations, including collinear periodic fractures in an infinite plane. The displacement profile for this particular geometry is given by

$$d = \frac{\omega}{G}\sigma\frac{W}{\pi}\cosh^{-1}\left[\frac{\cos(x\pi/W)}{\cos(a\pi/W)}\right], \tag{4}$$

where σ is the applied (remote) stress, W the distance between the crack centers (model width in the present study; Figure 2a), a the crack half length, G the shear modulus, and ω given by

$$\omega = 2(1-\nu) \quad \text{for plane strain,}$$
$$\omega = 2/(1+\nu) \quad \text{for plane stress.}$$

The maximum crack opening, that is, aperture, occurs at the crack center ($x = 0$) and given by

$$d_{max} = \frac{\omega}{G}\sigma\frac{W}{\pi}\cosh^{-1}\left[\sec\left(\frac{a\pi}{W}\right)\right]. \tag{5}$$

For a constant ratio of crack half length to crack center distance (a/W), the maximum aperture to crack center distance ratio (d_{max}/W) hence only depends on remote stress and elastic constants. Note that in the case of stepping (noncollinear) cracks, the maximum aperture depends, under constant driving stress conditions, also on overlap and separation (Olson, 2003; Pollard et al., 1982).

For a constant mode I fracture toughness (K_{Ic}), the maximum aperture at incipient failure is obtained by setting $K_I = K_{Ic}$ and substituting the stress intensity factor—remote stress relation ($K_I = f(\sigma)$) for this geometry (as given by equation (A6)) into equation (5)

$$d_{max} = \frac{\omega}{G}\frac{K_{Ic}}{\sqrt{W\tan\left(\frac{\pi a}{W}\right)}}\frac{W}{\pi}\cosh^{-1}\left[\sec\left(\frac{a\pi}{W}\right)\right], \tag{6}$$

which for an isolated crack (when $W \to \infty$) yields the plane strain solution given by equation (1) (with $G = E/[2(1+\nu)]$) so that aperture scales with the square root of the crack length under constant stress intensity factor conditions (as derived by Olson, 2003). For collinear periodic cracks with a constant crack half length to crack center distance ratio (a/W), aperture scales with the square root of the crack center distance (W), that is, the length scale. On the other hand, for a constant crack center distance, aperture scales with the square root of crack length only up to a certain a/W ratio, beyond which d_{max} asymptotically approaches zero as $2a \to W$ (Figure 3b).

We validated our lattice approach by running high-resolution models with constant crack center distance, that is, model width W, and varying crack half length a. The lattice models were extended until the first

bond failed. Displacement profiles and the maximum opening at incipient propagation are then compared with equations (4) and (6), respectively (Figure 3), for which the bulk properties listed in Table 1 are used. The results are in excellent agreement with LEFM solutions and illustrate, for example, that with increasing crack length the displacement profiles become flat-topped due to tip-to-tip fracture interaction (Figure 3a; see also Martel & Shacat, 2013). At this point it is also worth mentioning that for a periodic set of "stacked" parallel fractures of equal length and of constant spacing arranged like rungs on a ladder, the displacement profiles also become more flat-topped as spacing decreases (Martel & Shacat, 2013). Interestingly, in a nonperiodic array of such stacked fractures, the outermost fractures exhibit opening, whereas the inner fractures close once a critical spacing is reached, even though the array is subjected to remote extensional load (Germanovich & Astakhov, 2004), a result which has direct implications for the models presented later.

3.2. Aperture-to-Length Scaling of Nonpropagating Cracks

Noninteracting and nonpropagating opening mode fractures in a linear elastic medium subjected to a remote tension σ are expected to exhibit aperture-length ratios that only depend on remote stress and elastic constants (Pollard & Segall, 1987; Olson, 2003):

$$\frac{d_{\max}}{L} = \sigma \frac{2(1-\nu^2)}{E}. \tag{7}$$

Mechanical interaction will lead to deviations from this scaling law (Olson, 2003), as discussed below.

We tested our modeling approach by randomly positioning parallel cracks into the lattice model with crack lengths drawn randomly from a uniform size distribution with $L_{\min} = 10R$ and $L_{\max} = 100R$. The only restrictive condition evoked in the random crack placement is that the distance between the tips of two colinear cracks must be at least $6R$. The models are composed of 40,000 particles (200 particles per row; 200 rows). Cracks are randomly placed until a certain crack density is reached. Here we use the following definition of crack density widely used in effective medium theories and introduced by Bristow (1960):

$$\rho = \frac{1}{A}\sum_{i=1}^{n} a_i^2, \tag{8}$$

where A denotes the reference area, a_i the half-length of the ith crack, and n the number of cracks in A (Kachanov, 1992; Orlowsky et al., 2003). The squared crack half-length reflects the fact that the compliance contribution of the ith crack is proportional to its size squared (cubed in the case of circular shaped cracks in 3-D), a relation that however is strictly speaking only valid for noninteracting cracks (see critical comment by Kachanov, 2007). A selection of pre-cracked models (out of a total of 30 realizations) for two different fracture densities is shown in Figure 4a. Importantly, the predefined fracture densities used cover the range of densities observed in the fracture system models (section 3.3) in which fractures were not predefined but nucleated and propagated within a heterogeneous material.

The model boundaries are moved outward until a finite strain $\varepsilon_y = 10^{-4}$ is reached, and the tensile load σ_y (which is taken as the remote stress σ in the present context, although a strain boundary condition is used) is computed by dividing the summed out-of-balance forces of the boundary particles by the model width. The fractures' aperture-length data, normalized by particle diameter $2R$, are shown, together with the analytical expression for noninteracting and nonpropagating cracks (equation (7)), in Figure 4b. The results indicate that aperture-to-length scaling is approximately linear ($b \approx 1$) and therefore consistent with equation (7), reflecting that, on average, the competing effects of stress shielding and stress amplification cancel out (Kachanov, 1992). However, there is a hint that long cracks are typically "overdisplaced," meaning their apertures are greater than expected for an isolated (noninteracting) crack, reflecting stress amplification as expected for colinear cracks or stepping cracks with small overlap lengths relative to the crack length. On the other hand, short cracks appear to be slightly "underdisplaced" as they often lie in the stress shadows of larger cracks. These two effects lead to aperture-to-length scaling that is slightly superlinear, that is, $b > 1$. It is hence expected that in fracture systems with randomly located cracks that are not critically stressed, aperture-to-length scaling should be, on average, approximately linear or slightly superlinear.

The main purpose of the models illustrated in Figure 4a is investigating the aperture-to-length scaling of nonpropagating cracks. However, this series of models can also be used to compare the effective modulus normal to the cracks E_y with theoretical predictions from effective medium theory for randomly positioned parallel cracks (see section A5 for details). The results (Figure A4) indicate that so-called "differential schemes" fit

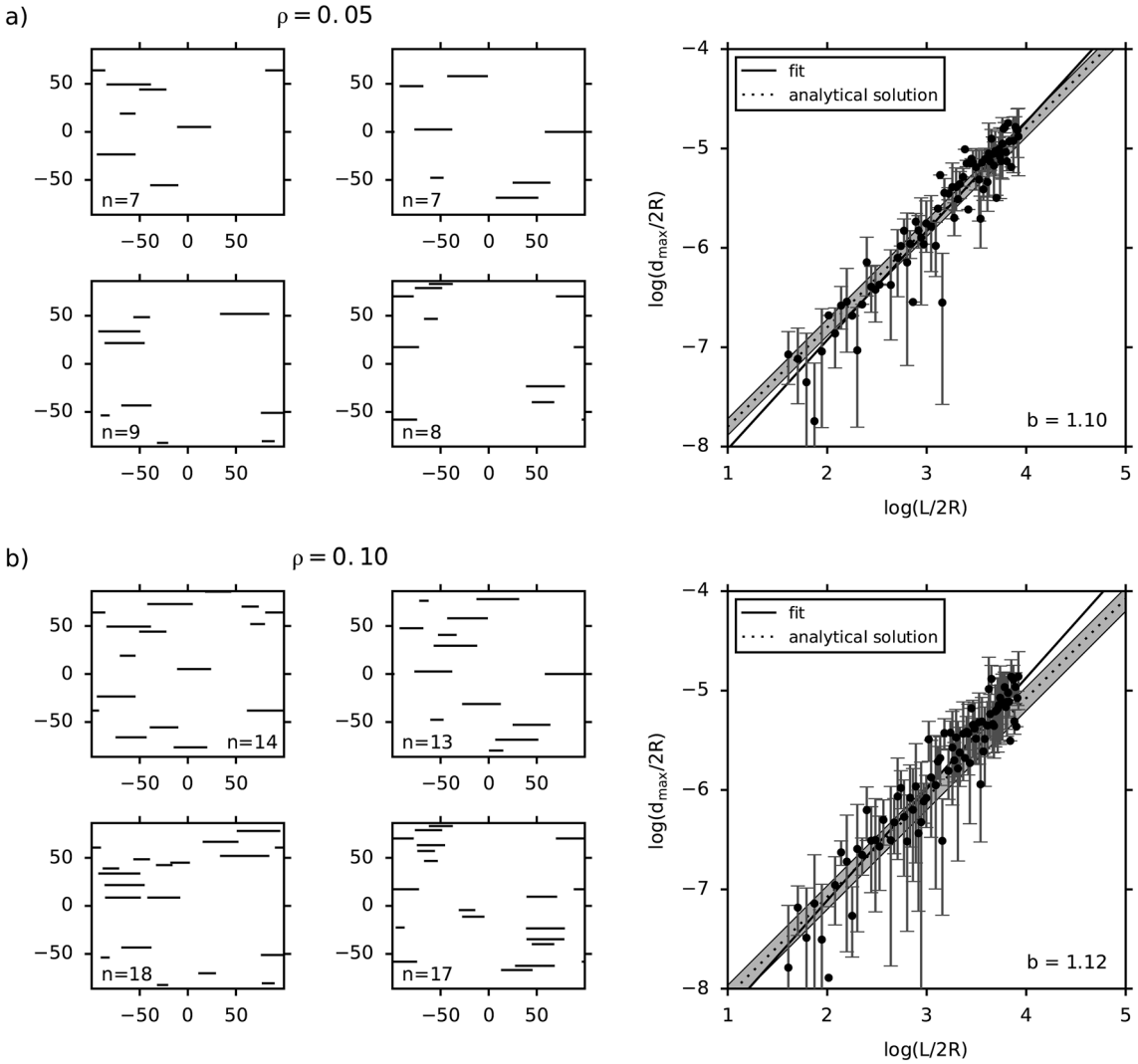

Figure 4. Scaling of predefined, nonpropagating cracks in models with fracture densities of (a) $\rho = 0.05$ and (b) $\rho = 0.1$ (as defined by equation (8)). In the left column, the crack patterns in four selected models (out of a total of 30) are shown (n is number of cracks). The fractures' aperture-length data (mean ± one standard deviation) from all realizations are compared with analytical solution (equation (7)). The tensile load σ_y at a finite strain $\epsilon_y = 10^{-4}$ is taken as a proxy for remote stress (dashed line is relation for the mean tensile load, gray patch spans ± one standard deviation). Solid lines are best-fit linear relations with slope, that is, power-law exponent, b.

the lattice model data well. Moreover, analysis of "outliers" indicates that stacked cracks lead to a less than average reduction in stiffness, whereas collinear cracks or narrow multiple-segment zones lead to a greater than average stiffness reduction, results that are again consistent with stress shielding and stress amplification, respectively. On average, however, these competing effects cancel out when and only when crack positions are random.

3.3. Fracture Systems Models

The purpose of earlier sections was to illustrate aperture-to-length scaling of predefined fractures and to validate our numerical modeling scheme. In this section we focus on the modeling of fracture systems in materials with various degrees of strength heterogeneity, which is implemented by randomly picking bond strengths from a Weibull distribution (see section 2.2 and Figure 2b). All models presented in this subsection are composed of 216,000 particles, with 600 particles per row and 360 rows. As in the earlier described models, extension is achieved by applying outward directed velocities to the bottom and top row of particles (monotonically increasing boundary displacements as considered by Segall, 1984). The tensile load σ_y (out-of-balance force of boundary particles divided by model width) is continuously monitored, and the locations of broken bonds is exported in regular intervals for later analysis. The finite strain is 2×10^{-4} at

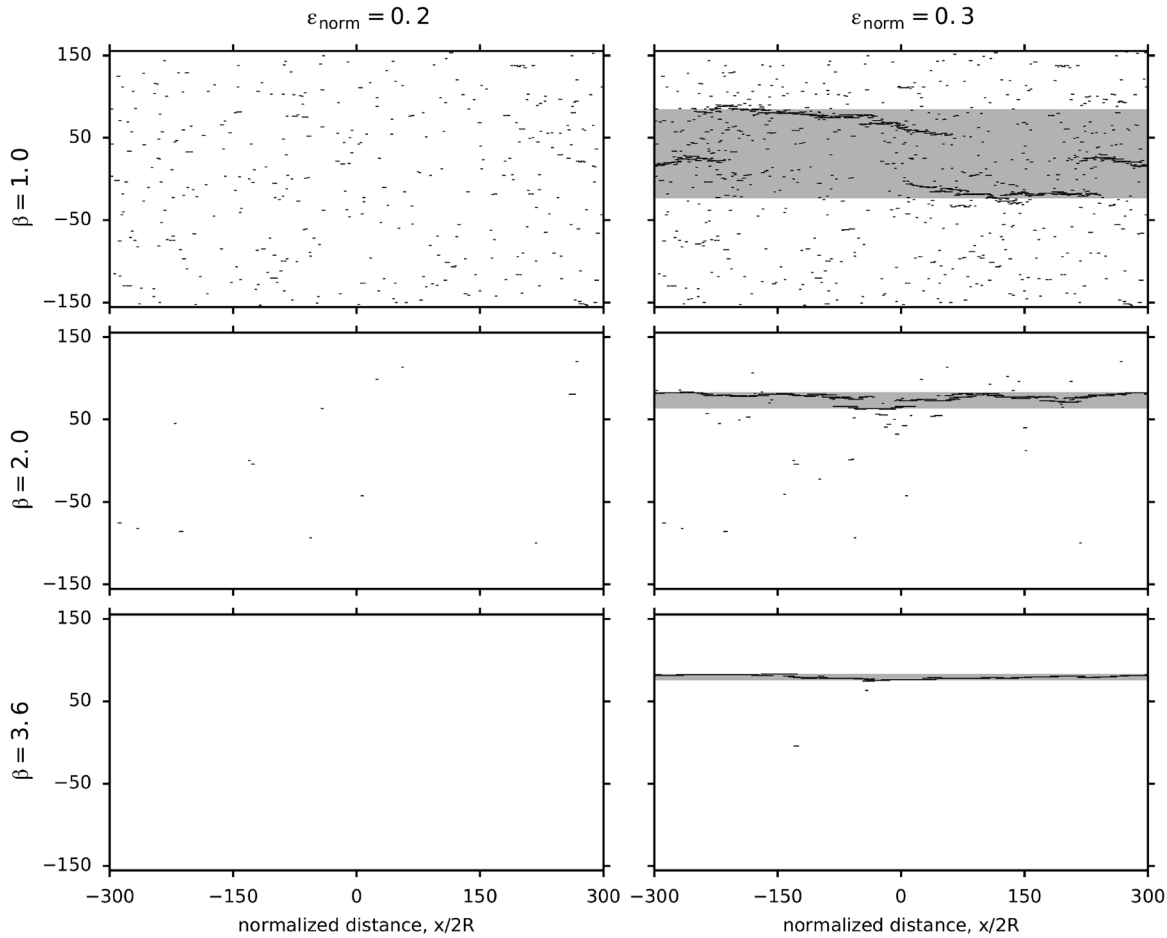

Figure 5. Modeled fracture systems for three different strength heterogeneities (decreasing with increasing Weibull shape parameters β) at a normalized strain ε_{norm} of 0.2 (left) and 0.3 (right). Gray patches in right column mark fracture zone width, which is determined by finding the maximum and minimum y position of those fractures with maximum apertures (d_{max}) exceeding the aperture at the changepoint x^* (see Figure 10b and text for further explanation).

which all models have significantly strain weakened. Model results are presented in terms of normalized strain, defined as $\varepsilon_{norm} = \varepsilon_y E/T$, where the tensile strength T is taken to be strength of a material without heterogeneity ($\beta \to \infty$). Similarly, the tensile load σ_y is normalized by the tensile strength T. Hence, in a perfectly homogeneous medium, failure occurs at $\varepsilon_{norm} = \sigma_y/T = 1$. All length measures are normalized by particle diameter $2R$.

3.3.1. Fracture Zone Development

Figure 5 shows the fracture patterns of two models (out of a total of 30 realizations) at two stages, namely, before ($\varepsilon_{norm} = 0.2$) and after ($\varepsilon_{norm} = 0.3$) the formation of fracture zones, which are highlighted as gray patches. Cumulative length-frequency distributions of fractures and fracture zone width data of all realizations are shown in Figures 6a and 6b, respectively. The fracture zone width was determined for each model by finding the maximum and minimum y position of those fractures with a maximum aperture d_{max} exceeding a certain cutoff value. As described later (section 3.3.2), fracture zone formation leads to nonuniversal aperture-to-length scaling, so that fractures with lengths greater than the changepoint (x^*, i.e., the kink in the bilinear relation for the logarithmic aperture-length data) exhibit sublinear scaling. The aperture at that

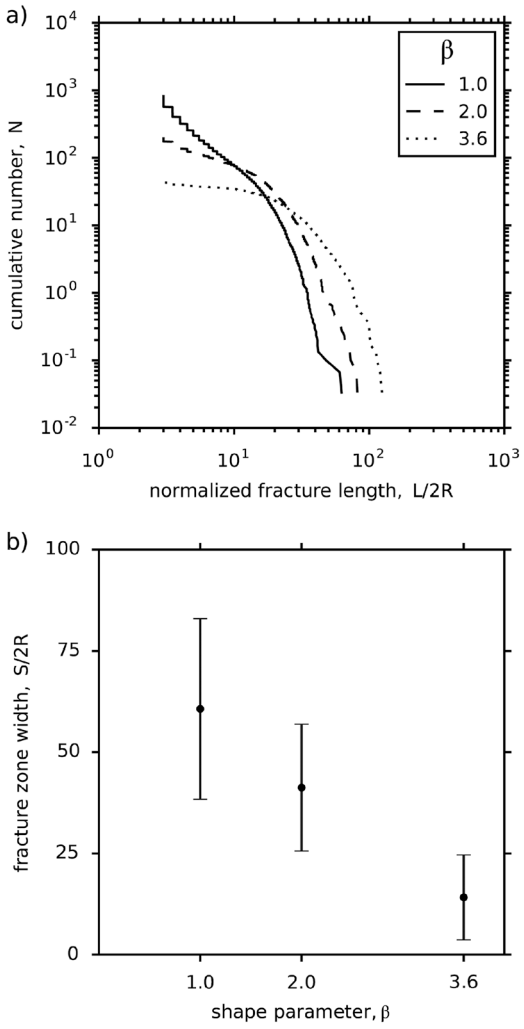

Figure 6. Influence of Weibull shape parameter β on fracture length distributions and fracture zone width (data from 30 realizations at a strain of $\varepsilon_{norm} = 0.3$). (a) Cumulative length-frequency distributions of fractures per model (the total fracture number N is normalized by the number of realizations). (b) Fracture zone width (mean ± one standard deviation) versus shape parameter.

changepoint, that is, $d_{max}(L = x^*)$, as given by the best-fit (strain-dependent) relation (Figures 10b and 10c), proofed to be a good choice for objectively determining fault zone width.

The models show, as perhaps expected, that in a relatively homogeneous material ($\beta = 3.6$), one narrow fracture zone composed of relatively long segments develops, whereas in a very heterogeneous material ($\beta = 1$), several stepping fracture zones composed of shorter segments form. The cumulative length-frequency distributions support this observation and show that with increasing strength heterogeneity, fracture lengths decrease, whereas the number of fractures increases (Figure 6a; average fracture densities are discussed later), a trend consistent with the results of Renshaw and Pollard (1994), who systematically varied initial flaw density. The width of the fracture zone, which always forms after the remote peak stress is reached, hence reflects material heterogeneity (Figure 6b). However, irrespective of material heterogeneity, ultimately always one geometrically and kinematically coherent zone develops due to the nature of the boundary condition used, that is, constant boundary displacement. In a natural system, such a fracture development is expected within a layer subjected to extension which is completely decoupled from its surrounding layers, implying either infinitely tall fractures or layers where the interfacial boundaries are frictionless and there is no top and bottom crack tip per se. The absence of possible 3-D effects (e.g., layer-confined fractures) on aperture-to-length scaling should hence be borne in mind in the interpretation of our models (e.g., lower aperture-length ratios for longer fractures, as shown by the pseudo-3-D models of Olson, 2003).

The evolution of a relatively narrow fracture zone from a $\beta = 3.6$ model is illustrated in Figure 7a. The displacement profiles clearly illustrate how displacement is transferred between segments along "rock bridges," so that the cumulative displacement resembles the profile of a single fracture (cf. to natural examples of Vermilye & Scholz, 1995). Clearly, many of the segments are overdisplaced and exhibit flat-topped displacement profiles as expected for crack arrays dominated by stress amplification. A detailed analysis of the aperture-to-length scaling of these multiple-segment zones that exhibit cumulative displacement distributions resembling those of a single fracture is however beyond the scope of the present study, which focuses on the scaling of individual segments. At this point it is worth recalling that our model approach permits only propagation within the plane of a crack, so that failure of bridges is inhibited, similar to earlier continuum-based studies (e.g., Olson, 2004; Renshaw & Pollard, 1994). This restriction is presumably the reason for the frequent development of fracture overlaps, although both field evidence and theoretical studies provide evidence for why cracks propagate straight past one another without intersection (Olson & Pollard, 1989, 1991) so that our approach is, for the small strains considered, justifiable. Because of this in-plane propagation, the fracture segments forming the zone exhibit strong interactions. Importantly, due to the displacement boundary conditions used, the maximum opening any fracture can exhibit equals the boundary displacement (bold horizontal lines in Figure 7a). This statement is obviously only true in our idealized two-dimensional models in which only one fracture zone develops and should therefore not be generalized. In natural systems composed of more than one fracture zone, the cumulative opening (e.g., as determined along a scan line) will provide an estimate of the extension accommodated by fractures. Ultimately, in our models the majority of fractures comprising a well-localized zone will have a maximum opening equal to the boundary displacement, irrespective of fracture length, implying that, in the limit, the scaling exponent approaches zero.

The fact that only one fracture zone develops is obviously a result of the boundary conditions and the 2-D nature of our approach; in 3-D, the model mimics a layer that is completely decoupled from its surrounding

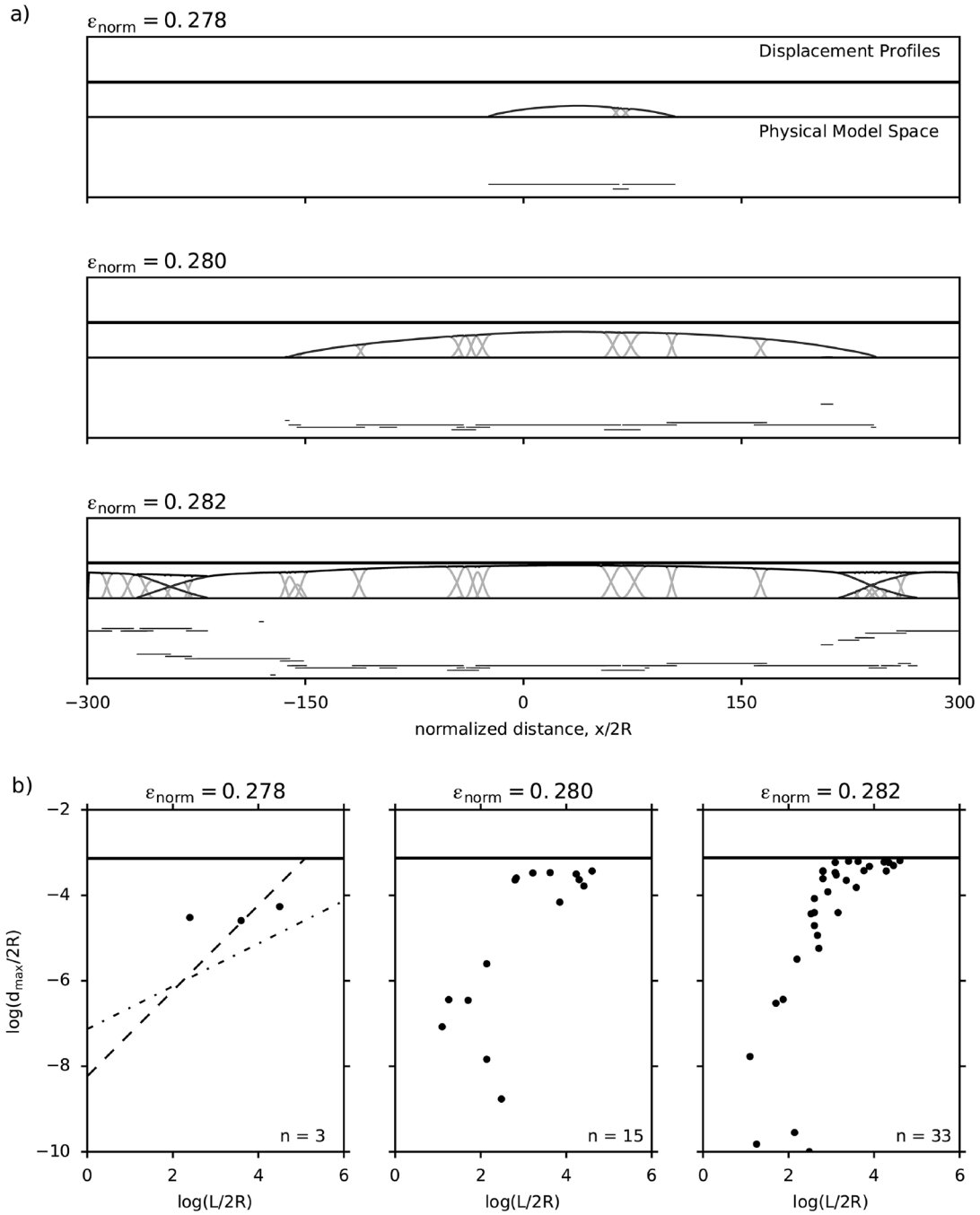

Figure 7. Evolution of a fracture zone within a $\beta = 3.6$ model. (a) Displacement profiles of individual fracture segments (light gray) and cumulative displacements (dark gray), together with the imposed boundary displacement (bold horizontal line). The fracture pattern in model space is shown under each displacement plot. (b) Maximum aperture versus fracture length graphs for the individual segments shown in (a). Solid horizontal line is the boundary displacement. The earliest stage shown ($\varepsilon_{norm} = 0.278$) is prior to peak stress; for this stage, the theoretical scaling for critically stressed and nonpropagating isolated fractures are shown as dash-dot and dashed lines, respectively (equations (1) and (7), respectively).

material (zero friction on layer boundaries leads to infinite spacing, i.e., one fracture, e.g., Schöpfer et al., 2011). However, this is possibly not the sole reason. For example, the degree of clustering and spacing between clusters relate to subcritical crack propagation parameters, as has been shown in 2-D and pseudo-3-D models (Olson, 1993, 2004, respectively). Future modeling with stress corrosion of the bonds (Potyondy, 2007) could show whether our particle-based lattice model produces similar results, namely, that clustering preferentially forms at a high subcritical index (Olson, 2004; Renshaw & Pollard, 1994).

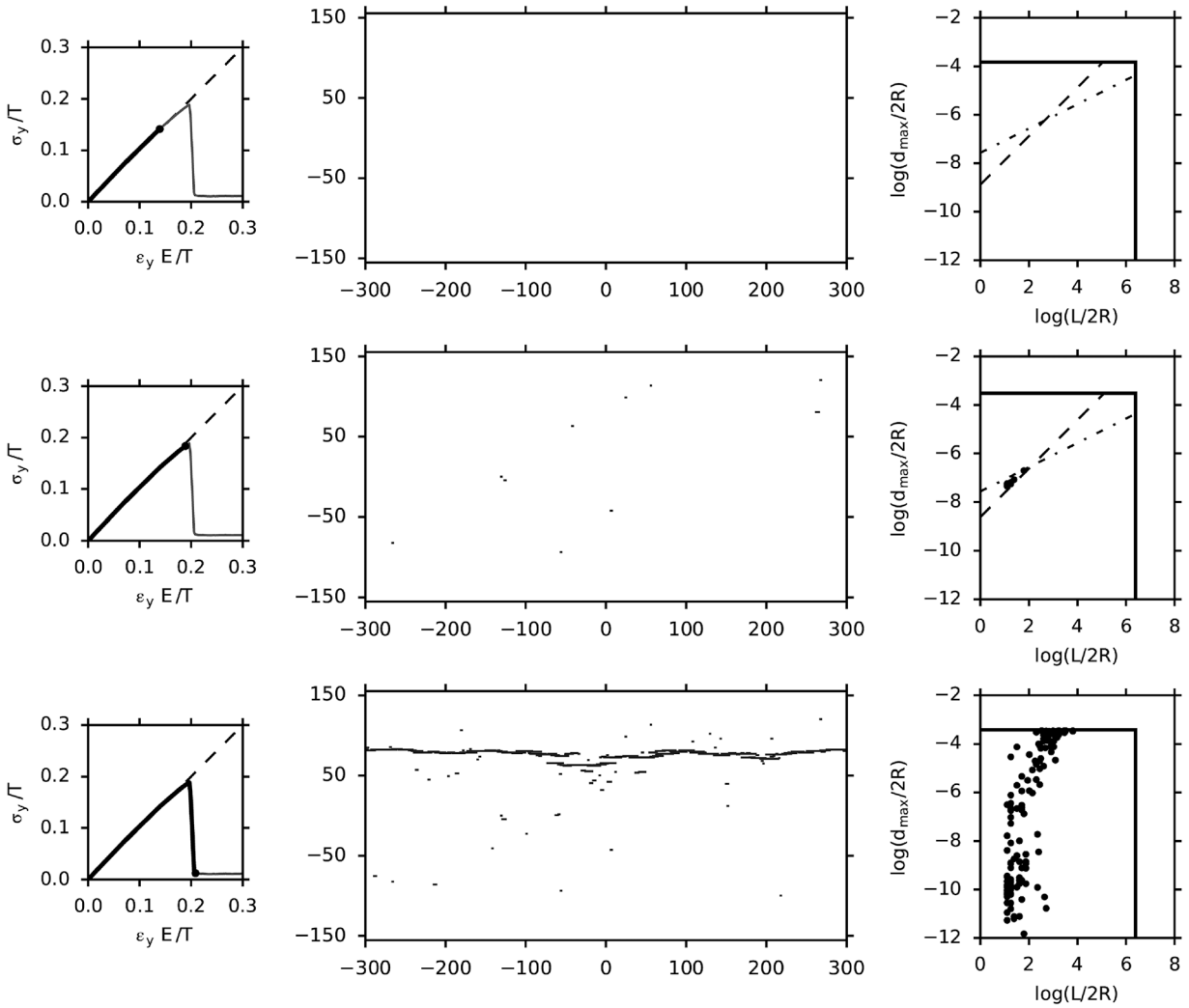

Figure 8. Evolution of a $\beta = 2$ model with strain increasing from top to bottom ($\varepsilon_{\text{norm}} = 0.173$, 0.193, and 0.217). In the left column, the system's normalized stress-strain response is shown (dot corresponds to stage shown; perfect elastic behavior is shown as dashed line). In the right column, the aperture-length data for all fractures are shown, together with the theoretical scaling for critically stressed and nonpropagating isolated fractures (equations (1) and (7), respectively) for the pre-peak stress stages. In the $d_{\text{max}} - L$ graphs, the imposed boundary displacement and the model width are shown as horizontal and vertical lines, respectively.

Aperture-length data for the fractures comprising a zone are illustrated in Figure 7b, together with the theoretical scaling relations for isolated cracks for the stage prior to peak stress, that is, max(σ_y). Clearly, after peak stress is reached, the tensile load cannot be taken as a proxy for driving stress and maximum opening of the segments comprising the zone approaches the boundary displacement, as discussed earlier. Although the number of fractures is relatively small at the last stage shown in Figure 7, one could argue for two scaling relations, a superlinear scaling for short fractures (with $L/2R \leq 20$) and a sublinear scaling (that may, in the extreme, yield a scaling exponent of zero) for longer fractures that take up most of the imposed boundary displacement. Clearly, a greater sample size is required for a robust statistical analysis of the scaling relations, as presented in the next section.

3.3.2. Universal and Nonuniversal Aperture-to-Length Scaling

In the preceding section we illustrated the formation of a localized fracture zone and presented aperture-length data from segments comprising such a zone. This section focuses on fracture scaling characteristic for a certain strength heterogeneity (as explained earlier, expressed in terms of Weibull shape parameter β) within the entire modeled fracture system. A robust statistical analysis however requires the analysis of multiple realizations, that is, models with identical statistical lattice properties, but different

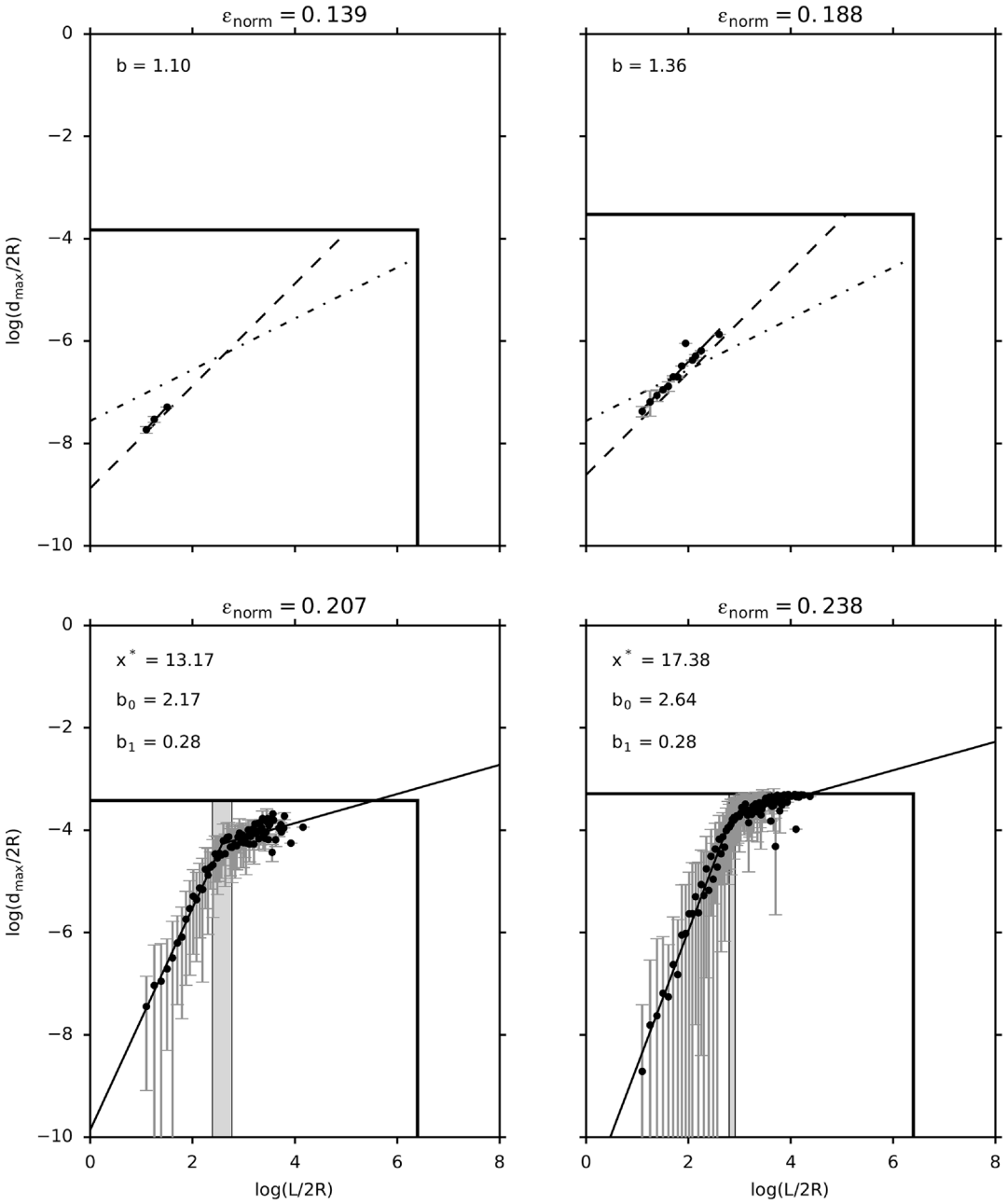

Figure 9. Aperture-length data from 30 realizations with $\beta = 2.0$ for four stages of normalized strain ε_{norm}. Dots are the mean values for each distinct fracture length, and error bars indicate ±one standard deviation. Prior to peak stress, the theoretical scaling for critically stressed and nonpropagating isolated fractures are shown (equations (1) and (7), respectively). The imposed boundary displacement and the model width are shown as horizontal and vertical lines, respectively. Prior to peak stress, data are fitted with a universal power-law scaling relation with exponent b, whereas after peak stress, nonuniversal scaling is observed (bilinear fit to logarithmic data) with exponents b_0 and b_1 (see equation (9)). For the latter case, the 95% confidence bounds around the changepoint x^* are shown as vertical gray bars.

sequence of random numbers used for assigning bond strengths (X in equation (3)). For each of the three β values used, 30 realizations were run, and the pooled data are analyzed.

Key stages of one of the $\beta = 2$ model realizations are shown in Figure 8, together with the system's normalized stress-strain response and the aperture-length data. At peak stress, aperture-to-length scaling is clearly linear, and the fractures' aspect ratios (d_{max}/L) are slightly larger than for a nonpropagating isolated frac-

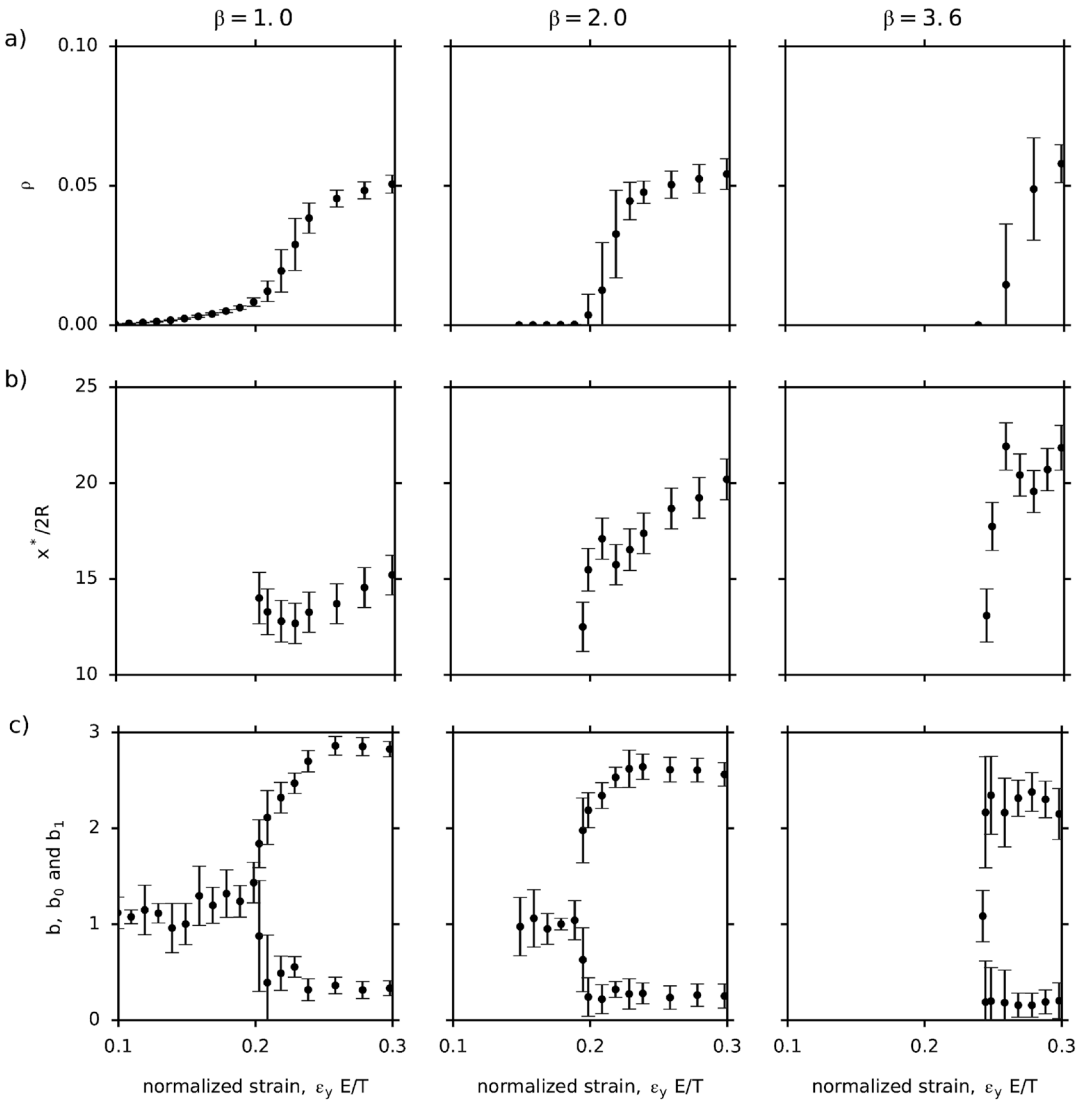

Figure 10. Fracture densities and results of best-fit universal and nonuniversal aperture-to-length scaling as a function of normalized strain for three different strength heterogeneities (expressed as Weibull shape parameter β). (a) Fracture density ρ (as defined by equation (8)) plotted as mean ± one standard deviation. (b) Changepoints x^*. (c) Slopes b, b_0, and b_1. In (b) and (c), each best-fit parameter is plotted as point with error bar representing the 95% confidence bound.

ture (equation (7)). Shortly after peak stress, a localized zone develops (as shown for all β values used in Figure 5) and aperture-to-length scaling becomes clearly nonlinear.

The pooled data for the $\beta = 2$ models are shown in Figure 9, together with scaling relations for isolated fractures. Prior to peak stress, the (average aperture) data are well-fitted with a universal scaling relation. After peak stress, however, a bilinear relation is fitted to the logarithmic data. The relation has the form (Main et al., 1999)

$$f(x_i) = a_0 + b_0 \quad [x_i \quad I(x_i < x^*) + x^* \quad I(x_i \geq x^*)] + b_1(x_i - x^*)I(x_i \geq x^*), \tag{9}$$

where a_0 is the intercept, b_0 and b_1 are the slopes, x^* is the changepoint, and I is the indicator function; if the inequality in the brackets holds, then $I = 1$, otherwise $I = 0$. Fitting is performed using nonlinear least squares as implemented in Matlab (lower/upper bound for x^* is taken as the third smallest/largest value; lower/upper bound for the b's is 0/5 and for a_0 it is $-\infty/+\infty$). Note that the same procedure was used to fit the data shown in Figures 1a and 1b, which gives identical results (within the confidence bounds) to the best-fit relations given in Main et al. (1999) and Renshaw and Park (1997), respectively.

The best-fit parameters for the three different β-value models are shown as a function of normalized strain in Figures 10b and 10c. Additionally, the fracture density (as defined by equation (8)) is shown as a function of strain, where the reference area A is taken to be the total model area. Prior to peak stress, that is, the formation of a fracture zone, the scaling exponent b is approximately 1.0 (in the least heterogeneous model, i.e., $\beta = 3.6$, insufficient pre-peak-stress data are available). This linear (or slightly superlinear; $b > 1$) scaling relation, together with the low fracture densities ($\rho < 0.01$), suggests that prior to peak-stress, the majority of fractures are noninteracting and not critically stressed (section 3.2). Fracture densities increase during fracture zone formation, where the most heterogeneous material ($\beta = 1$) shows the "smoothest" increase. After fracture zone formation, the best-fit bilinear relation (equation (9)) yields changepoint values that increase with model extension and decrease with increasing strength heterogeneity. As illustrated in Figure 7, the changepoint corresponds to the shortest fracture comprising the fracture zone that accommodates the imposed boundary displacement. The shortest zone-forming fracture clearly decreases with increasing strength heterogeneity (see also Figure 6a). In other words, the changepoint magnitude "represents the maximum length scale at which the apertures of smaller fractures are affected by stress perturbations induced by larger fractures," as argued by Renshaw and Park (1997). Interestingly, Renshaw and Park (1997) used a constant remote stress boundary conditions, whereas in our models a uniform boundary displacement is specified (which arguably is more appropriate for the field data described by Hatton et al., 1994), yet a similar bilinear scaling develops as the fractures interact, suggesting that this effect does not depend on the nature of the boundary condition or the fracture growth rule.

Fracture densities are very similar after zone localization ($\rho \approx 0.05$), although a slight increase with decreasing heterogeneity is evident and in fact expected (a single fracture spanning the entire model would lead to a fracture density $\rho = (W/2)^2/(WH) \approx 0.5$). If the fractures were randomly located, then weak interactions are expected for these relatively low fracture densities, that is, the effects of stress shielding and stress amplification cancel out (see section 3.2 and Figure 4). This is clearly not the case in the fracture system models, which do show clustering and hence locally high crack densities resulting in strong interactions.

The best-fit slope b_1 of the bilinear relation is typically <0.5 and increases with increasing strength heterogeneity (decreasing β value). Again, this is consistent with the formation of fracture zones, which become narrower and better localized in more homogeneous materials. As postulated earlier, in the extreme case, all fractures comprising the zone have a maximum aperture equal to the boundary displacement that is independent of fracture length ($b_1 \to 0$; see also Figure 7). Clearly, the sublinear scaling of the longer fractures ($L > x^*$) cannot be interpreted in terms of the propagation of an individual crack (Scholz, 2011) but reflects strong segment interaction (Pollard et al., 1982). On the other hand, the superlinear scaling relation of the shorter fractures, with scaling exponents b_0 ranging from 2 to 3, is due to stress shielding in the material outside of the fracture zone.

3.3.3. Implications for the Interpretation of Natural Fracture Systems

Finally, it seems appropriate to discuss the preservation potential of these aperture-to-length scaling relations (see also in-depth discussion by Olson, 2003). In the present models, the linear scaling prior to strong segment interaction is "lost" after fracture zone formation due to crack closure, a scenario which in natural systems may be possible if the fractures are fluid filled or empty and if the host rock behaves elastically. Mineralization of fractures (or crystallization of the fluid inside the fractures) could inhibit fracture closure and hence preserve the early aperture-to-length scaling, so that the relatively large scaling exponents (b_0 ranging from 2 to 3) cannot develop and the linear scaling is preserved. On the other hand, the sublinear aperture-to-length scaling of the long fractures comprising the multiple-segment fracture zones is expected to be preserved, even when the stress induced by the (remote tectonic) extension is relaxed. This sublinear scaling, when encountered in the field, should however not be necessarily interpreted to reflect a preserved active subcritical or critical propagation state, since such scaling can also result from strong segment interaction under tectonic extension, as shown in the present study.

4. Conclusions

Using a simple lattice model, which is consistent with LEFM, quasi-static fracture systems restricted to in-plane fracture propagation under constant displacement boundary conditions were modeled that lead to the following principal conclusions:

1. Prior to the formation of a fracture zone, aperture-to-length scaling is linear or slightly superlinear, suggesting that in a heterogeneous material, the majority of fractures are not critically stressed and that effects of fracture interaction (shielding and amplification) cancel out.
2. After the formation of a segmented fracture zone, aperture-to-length scaling becomes nonuniversal, with long fractures comprising the multiple-segment zone exhibiting sublinear scaling and short fractures exhibiting superlinear scaling.
3. The length scale at which a change from superlinear to sublinear aperture-to-length scaling occurs increases with increasing extension and is therefore not related to a preexisting structure but reflects the shortest segments that comprise the multiple-segment fracture zone.
4. The two competing effects of stress shielding and stress amplification, which typically cancel out up to high crack densities when fractures are randomly located, lead to nonuniversal aperture-to-length scaling in clustered fracture systems, where the long (colinear or stepping) fractures comprising the fracture zone are dominantly affected by stress amplification and the shorter fractures in the stress shadow of the zone are dominantly affected by stress shielding.

Appendix A: Bulk Properties of Lattice Model

A1. Introduction

In this appendix the bulk properties, such as elastic constants, tensile strength, and mode I fracture toughness, of the lattice model are described. The elastic properties and strength are determined using fully bonded models with constant bond strength. The inverse form of Hooke's law for plane strain is

$$\begin{aligned}\varepsilon_x &= \frac{(1-\nu^2)}{E}\sigma_x - \frac{\nu(1+\nu)}{E}\sigma_y,\\ \varepsilon_y &= \frac{(1-\nu^2)}{E}\sigma_y - \frac{\nu(1+\nu)}{E}\sigma_x,\end{aligned} \tag{A1}$$

where E is the Young's modulus, ν the Poisson's ratio, and the x and y axes are principal axes of stress and strain (σ and ε, respectively). In the present setup, periodic boundaries are used in the x direction so that $\varepsilon_x = 0$. The nonzero strain and stress in the y direction, ε_y and σ_y, are readily computed from the model boundary displacement and the tensile load, respectively. The stress in the x direction σ_x, which has under $\varepsilon_x = 0$ conditions the same sign as σ_y if $\nu > 0$, is computed using an averaging procedure that permits estimating continuum quantities (such as stress) from discrete media (so-called measurement circle; Potyondy & Cundall, 2004). This circular averaging region is positioned in the model center and has a radius equal to 45% of the minimum model dimension, that is, $0.45\min(W, H)$, where W and H is the model width and height, respectively. From these nonzero quantities (ε_y, σ_y, and σ_x), the effective elastic constants of the lattice are then readily obtained from equation (A1). For the fracture toughness tests, a preexisting crack is defined in the model center (as illustrated in Figure 2a).

As explained in section 2.1, our model approach differs from earlier mass-spring-damper models because of the usage of finite width inter-particle bonds (so-called "parallel bonds"; Potyondy & Cundall, 2004). These bonds provide a more realistic behavior since in addition to forces, a moment can develop at bonded particle-particle contacts, leading to a fundamentally different behavior which is best illustrated by the deformation of rock bridges between two overlapping fractures. Figure A1 shows the fractures' opening displacement profiles for the "classical" linear contact bond model (1-D spring) and the parallel bond model (finite width cement) used in the present study. The predefined fractures have a separation equal to one particle diameter, meaning that the rock bridge is a string of bonded particles. Without any bending resistance, the displacement profiles along the rock bridges are linear.

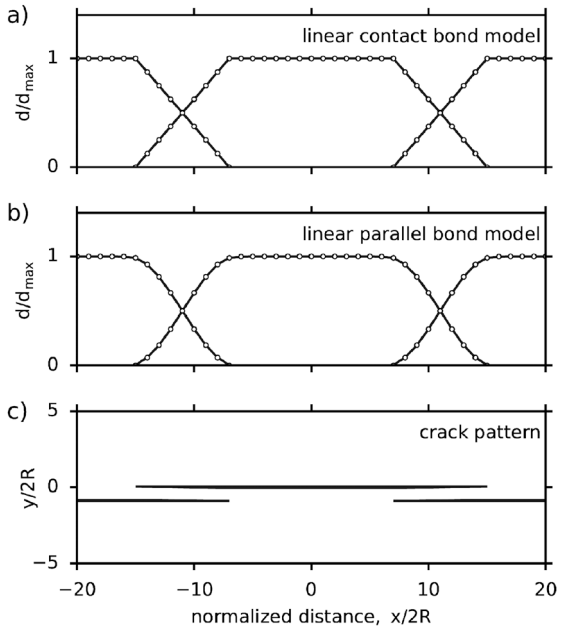

Figure A1. Comparison of "classical" 1-D spring contact model (so-called "linear contact bond model") and bonds with finite width (so-called "linear parallel bond model"). See Potyondy and Cundall (2004) for implementation details. An infinitely long array of overlapping fractures is predefined in the lattice model with a fracture separation equal to one particle diameter (fracture geometry is illustrated in (c)). Infinite bond strength provides fully elastic behavior. The 1-D spring model leads to linear displacement profiles (a), whereas the finite width bond provides nonlinear (tapered) profiles as expected for a beam (b). Crack displacements are normalized by boundary displacement.

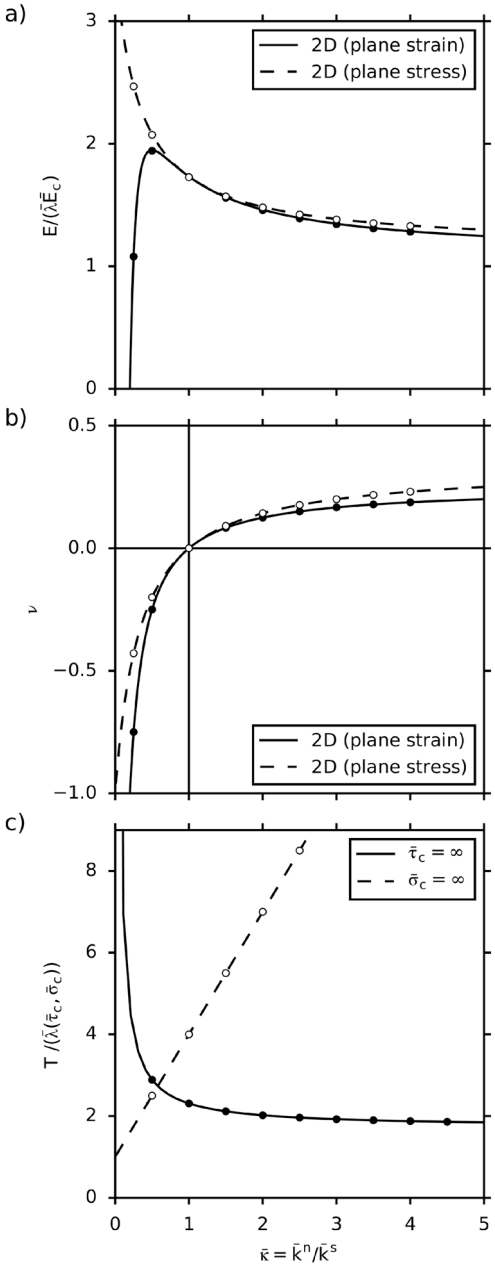

Figure A2. Effective properties of particle-based lattice solid model under extension as a function of the bond stiffness ratio $\bar{\kappa}$. (a) Normalized Young's modulus, (b) Poisson's ratio, and (c) normalized tensile strength. Analytical solutions are shown as curves and numerical model results as dots. Elastic properties are plotted for plane strain and plane stress conditions (equations (A2) and (A3), respectively). The normalized tensile strength is shown for two cases, infinite bond shear strength ($\bar{\tau}_c = \infty$; equation (A4)) and infinite bond tensile strength ($\bar{\sigma}_c = \infty$; equation (A5)).

On the other hand, the parallel bond model provides the behavior of a (linear elastic) beam and therefore nonlinear (tapered) displacement profiles along the rock bridges. Hence, even when the fracture separation is equal to one particle row, realistic bulk behavior is achieved.

A2. Effective Elastic Properties of Intact Lattice

The effective elastic properties of a triangular lattice composed of linear elastic springs can be expressed analytically (Bathurst & Rothenburg, 1988; Griffiths & Mustoe, 2001; Liu et al., 2013; Rothenburg et al., 1991; Toomey & Bean, 2000; Wang & Mora, 2008). Here we adapt existing relations to take into account the finite bond width using the notation given by Potyondy and Cundall (2004) and assuming equisized discs of radius R and unit thickness: The bond width $2\bar{R}$ is set by the so-called bond width multiplier, $\bar{\lambda} = \bar{R}/R$. The axial bond stiffness $\bar{k}^n$ is set with the bond modulus via the relation $\bar{E}_c = 2R\bar{k}^n$ (note that $2R$ is the beam length), and the tangential stiffness $\bar{k}^s$ is set with the bond stiffness ratio, $\bar{\kappa} = \bar{k}^n/\bar{k}^s$. These relation then lead to the following relations between the bond properties $\bar{\lambda}$, $\bar{E}_c$, and $\bar{\kappa}$ and the effective Young's modulus E and Poisson's ratio ν:

$$E = \bar{\lambda}\bar{E}_c \frac{\sqrt{3}}{8}\frac{(5\bar{\kappa}-1)(\bar{\kappa}+1)}{\bar{\kappa}^2}, \nu = \frac{\bar{\kappa}-1}{4\bar{\kappa}} \quad \text{for plane strain,} \tag{A2}$$

$$E = \bar{\lambda}\bar{E}_c 2\sqrt{3}\frac{\bar{\kappa}+1}{3\bar{\kappa}+1}, \nu = \frac{\bar{\kappa}-1}{3\bar{\kappa}+1} \quad \text{for plane stress.} \tag{A3}$$

These analytical relations are plotted as a function of stiffness ratio $\bar{\kappa}$ in Figures A2a and A2b and compared with results obtained from tension tests on the numerical lattice model. It is worth recalling that a positive Poisson's ratio requires $\bar{\kappa} > 1$ (Gaspar, 2010; Rothenburg et al., 1991) and that the maximum achievable Poisson's ratio (as $\bar{\kappa} \to \infty$) in a triangular lattice model is $\nu = 1/4$ and $\nu = 1/3$ for plane strain and plane stress conditions, respectively. Note that in a square lattice with bonds parallel/normal to the extension direction $E = \bar{\lambda}\bar{E}_c$ and $\nu = 0$ (the square lattice is however orthotropic and hence not suited for modeling linearly isotropic elastic solids).

A3. Tensile Strength

The maximum tensile and shear stresses acting on the parallel-bond periphery are calculated from beam theory (equation 16 in Potyondy & Cundall, 2004). If the maximum tensile stress exceeds the tensile strength $\bar{\sigma}_c$ or the maximum shear stress exceeds the shear strength $\bar{\tau}_c$, then the parallel bond breaks, and it is removed from the contact along with its accompanying force, moment, and stiffnesses (after failure, a linear contact model with zero contact friction is assigned so that the "fracture wall" has a stiffness in case of crack closure). The lattice's tensile strength T under extension for the lattice orientation relative to the extension direction as shown in Figure 2a is given by

$$T = \bar{\lambda}\bar{\sigma}_c \frac{1}{\sqrt{3}}\left(3 + \frac{1}{\bar{\kappa}}\right) \quad \text{for} \quad \bar{\tau}_c = \infty, \tag{A4}$$

$$T = \bar{\lambda}\bar{\tau}_c(3\bar{\kappa}+1) \quad \text{for} \quad \bar{\sigma}_c = \infty. \tag{A5}$$

These equations indicate that when $\bar{\sigma}_c = \bar{\tau}_c$, bonds fail in tension when $\bar{\kappa} > 1/\sqrt{3}$ (Figure A2c). In the limit (when $\bar{\kappa} \to \infty$ and all load is carried in tension), the normalized tensile strength $T/(\bar{\lambda}\bar{\sigma}_c)$ approaches $\sqrt{3}$. Note that in a square lattice with bonds parallel/normal to the extension direction, $T/(\bar{\lambda}\bar{\sigma}_c) = 1$.

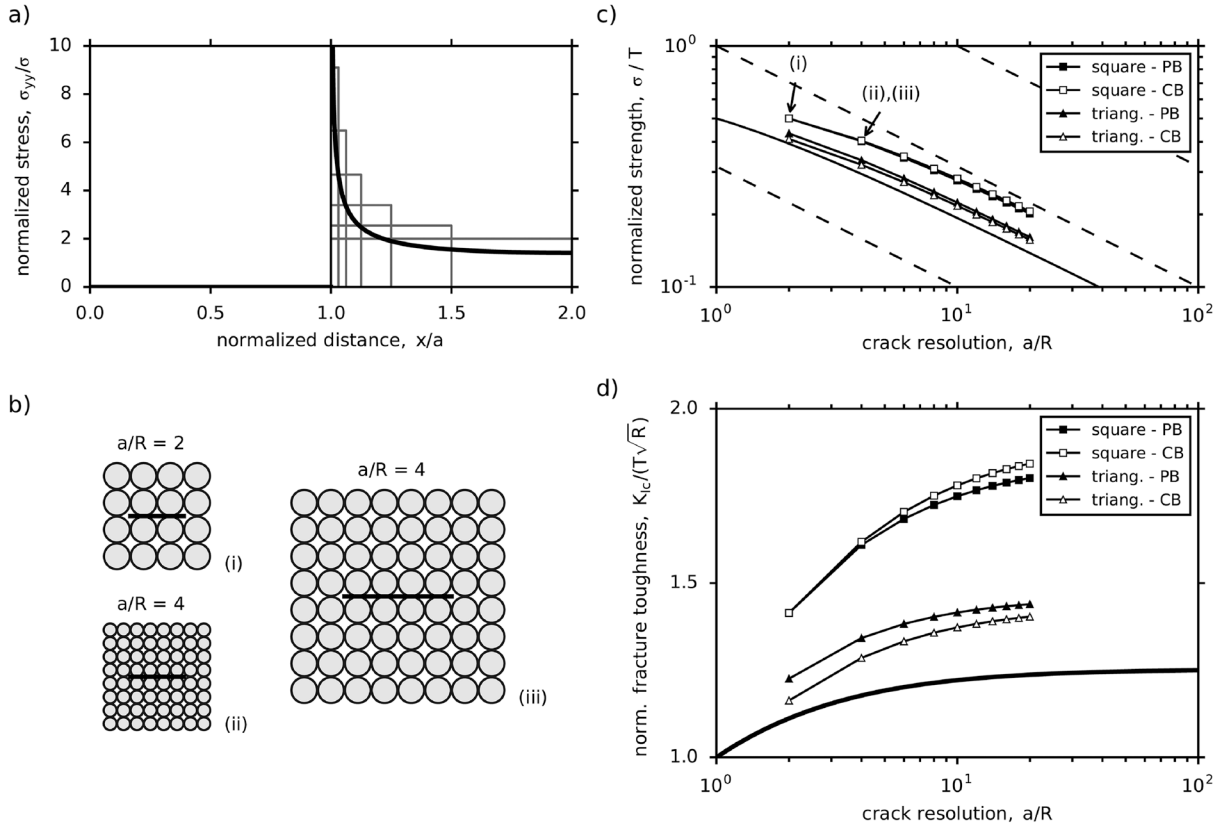

Figure A3. Mode I fracture toughness of lattice models. (a) Normal stress profile ahead of crack σ_{yy} normalized by remote stress σ (solid curve) for $a = W/4$ (equation (A7)). The boxes illustrate average normalized stress for different integration limits. (b) Illustration of dual-model similarity with square lattices. Identical sample strength and fracture toughness is obtained for models (ii) and (iii). (c) Normalized sample strength versus model resolution a/R for square and triangular lattices with contact bonds (CB) and parallel bonds (PB). Dashed lines have a slope of −0.5. The solid thick curve is an estimate based on stress integration ahead of the crack tip (as illustrated in (a)). For example, for $a/R = 2$ (as illustrated in (i)), the average normalized stress ahead of the crack tip equals 2.54, that is, the height of the box in (a) ranging from $x/a = 1$ to 1.5. On the basis of this simple analysis, the sample's normalized strength is hence expected to be $1/2.54 = 0.39$. (d) Normalized fracture toughness calculated using the data shown in (c).

A4. Fracture Toughness

The mode I fracture toughness is determined numerically by predefining fractures in the model center as schematically shown in Figure 2a. Since periodic boundaries are used, the predefined cracks (of half-length a) are colinear and periodic (the model width W is hence the distance between the crack centers). The stress intensity factor for this geometry is given by the following closed-form solution (e.g., Gross & Seelig, 2011)

$$K_I = \sigma\sqrt{W\tan\left(\frac{\pi a}{W}\right)}, \tag{A6}$$

where σ is the remote tensile stress. Note that with increasing width, the well-known solution for an isolated crack is obtained as $W \to \infty$, that is, $K_I = \sigma\sqrt{\pi a}$. The normal stress within the plane of the colinear periodic cracks is given by (e.g., Schijve, 1996; Figure A3a)

$$\frac{\sigma_{yy}}{\sigma} = \frac{\sqrt{2}\sin(\alpha x)}{\sqrt{\cos(2\alpha a) - \cos(2\alpha x)}}, \text{where} \quad \alpha = \frac{\pi}{W}, \tag{A7}$$

which illustrates the well-known fact that continuum mechanics solutions for cracks in a linear elastic medium predict stress singularities at the crack tip (at $x = a$; the crack center is at the origin). Such stress singularities do not arise in lattice models, because the integral stress ahead of the crack tip is carried by discrete bonds. A consequence of this discretization is that the fracture toughness depends on resolution, that is, number of particles or bonds per crack length, as documented for DEM models similar to those presented here (Potyondy & Cundall, 2004) and the macroscopic properties of microarchitectured materials (see review by Fleck et al., 2010).

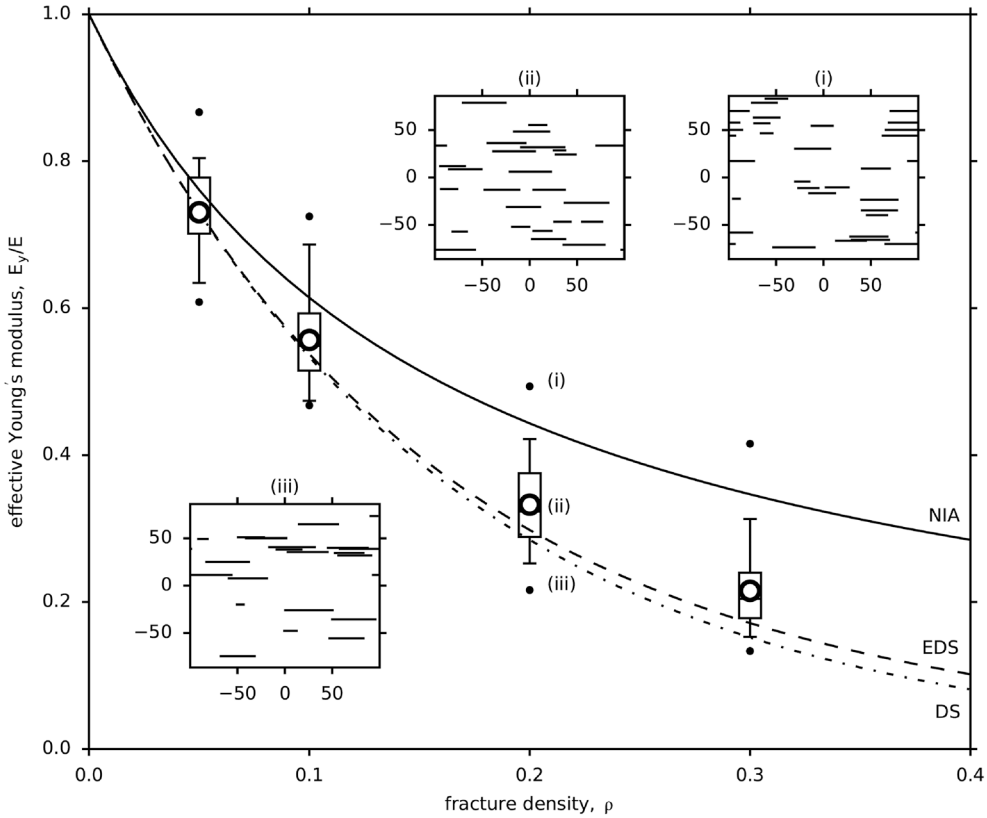

Figure A4. Effective Young's modulus normal to the cracks E_y normalized by the modulus of the intact material E versus fracture density ρ for the models described in section 3.2. Curves are theoretical predictions taken from the noninteraction approximation (NIA), the differential scheme (DS), and the extension of the differential scheme (EDS). Data ($n = 30$ per density) are plotted as a box and whisker diagram, where the boxes span from the 0.25 to 0.75 percentile and the whiskers from the 0.05 to 0.95 percentile. Median values are plotted as bold horizontal lines in each box, mean values as white points, and outliers as black points. The insets show the crack patterns for selected $\rho = 0.2$ models: (i) maximum; (ii) median; and (iii) minimum. Note "stacked" cracks in (i) and narrow zone in (iii), which both were generated by chance (i.e., by random positioning of cracks).

An approximate relation between the strength of a cracked specimen (and therefore fracture toughness) and model resolution can be obtained by computing the integral stress, or force, ahead of the crack tip as a function of distance from the crack tip. The indefinite integral of equation (A7) is

$$\int \frac{\sigma_{yy}}{\sigma} dx = -\alpha^{-1} \sin^{-1} \frac{\cos(\alpha x)}{\cos(\alpha a)} + C, \tag{A8}$$

where C is the integration constant. The definite integral from a (= position of crack tip) to $a + \Delta x$, with Δx being the distance ahead of the crack tip, is

$$\int_a^{a+\Delta x} \frac{\sigma_{yy}}{\sigma} dx = \frac{W}{2} - \alpha^{-1} \sin^{-1} \frac{\cos[\alpha(a + \Delta x)]}{\cos(\alpha a)}, \tag{A9}$$

which is hence equal to the maximum force $F_n^{\max}$ acting ahead of the crack tip on a line segment of length Δx (equivalent to particle diameter in a square lattice; Potyondy & Cundall, 2004). Normalizing of equation (A9) by Δx hence provides the average stress ahead of the crack tip (Figure A3a) and its inverse an estimate of the specimen's normalized strength, σ_y/T (Figure A3c). Clearly, the average stress ahead of the crack tip increases with decreasing Δx so that the specimen's strength decreases with increasing model resolution (Figure A3c).

From the above continuum-based analysis, it is clear that fracture toughness will depend on model resolution. Based on a similar analysis, Potyondy and Cundall (2004) postulated that for a given size of a BPM

$$K_{Ic} = T\sqrt{\pi\bar{\alpha}R}, \tag{A10}$$

where T is the tensile strength of the ensemble, and $\bar{\alpha}$ is a dimensionless factor that depends on particle packing, bond-strength heterogeneity, and other things (see also Cundall & Detournay, 2017; Huang & Detournay, 2008). Note that the relation between fracture toughness and internal length scale was derived on the basis of forces, rather than surface energy (as in the Griffith criterion, e.g.), which is more usual in fracture mechanics.

Consequently, a series of models (with $a = W/4$) and varying crack resolution (a/R) was run using both square and triangular lattices and both contact (1-D spring) and parallel (finite sized cement) bonds (results from square lattice models are simply shown for comparison; as stated in section 2.1, a square lattice is elastically orthotropic and was hence not used for the models shown here). In these models the applied stress at which the first bond breaks is taken as the strength of the cracked specimen, which is normalized by the tensile strength of equivalent uncracked specimens, that is, σ_y/T. Note that identical model results are obtained for models in which R is kept constant and W is varied and for models in which W is kept constant and R is varied (so-called dual-model similarity; Potyondy & Cundall, 2004; Figure A3b). It is hence useful to express the specimen's mode I fracture toughness in dimensionless form, that is, $K_{Ic}/(T\sqrt{R})$ (Figure A3d). As already noted by Potyondy and Cundall (2004), the strength versus resolution relations asymptotically approach a slope of minus one half (as expected from equation (A10)), so that the normalized fracture toughness asymptotically approaches a constant value at high model resolutions. Note that for the triangular lattice used here, the fracture toughness increases with resolution by a factor < 1.5.

A5. Effective Elastic Properties of Lattice Containing Parallel Fractures

The models run for investigating aperture-to-length scaling of randomly placed parallel fractures (section 3.2 and Figure 4) also provide interesting results regarding the effective elastic properties. An elastic solid containing parallel fractures is a transversely isotropic material (Kachanov, 1992) for which the plane strain-stress relation can be written as

$$\begin{aligned} \epsilon_x &= \frac{(1-\nu^2)}{E_x}\sigma_x - \frac{\nu(1+\nu)}{E}\sigma_y, \\ \epsilon_y &= \frac{(1-\nu^2)}{E_y}\sigma_y - \frac{\nu(1+\nu)}{E}\sigma_x, \end{aligned} \tag{A11}$$

where E_x and E_y are the effective Young's moduli in the x and y directions (which are planes of symmetry in the orthotropic solid) and E and ν are the elastic constants of the unfractured material (matrix; e.g., Kushch et al., 2009; Orlowsky et al., 2003). The effective moduli are determined from the pre-fractured models in the same fashion as for the intact lattice (as described in section A1), and the properties of the intact solid are computed using the plane strain analytical solutions (equation (A2)).

For one set of parallel fractures, Kachanov (1992) discusses three different theoretical descriptions, the noninteraction approximation, the differential scheme, and the extension of the differential scheme (see also summary in Orlowsky et al., 2003). For a solid containing a set of randomly distributed parallel cracks aligned with the x direction, all three theories predict that $E_x = E$, whereas $E_y = E/(1 + 2\pi\rho)$ (noninteraction approximation), $E_y = E\exp(-2\pi\rho)$ (differential scheme), and $E_y = E/[1+2\pi\rho\exp(\pi\rho)]$ (extension of the differential scheme), with ρ being the fracture density as defined by equation (8). The normalized effective moduli E_y/E obtained from the lattice models illustrate that, on average, the differential schemes provide the best fit, a result consistent with existing studies (Kushch et al., 2009; Orlowsky et al., 2003). The scatter is however significant, given the relatively small number of fractures per model and the large range of fracture lengths (see Figure 4). Nevertheless, outliers do illustrate that stacked cracks lead to stress shielding resulting in a lower than average reduction of E_y, whereas cracks aligned in a narrow zone lead to stress amplification causing a greater than average reduction of E_y (inset (i) and (iii) in Figure A4, respectively) as predicted by theory (Kachanov, 2007) and shown by existing studies (Orlowsky et al., 2003). Clearly, the formation of a fracture zone composed of colinear and stepping segments is the cause for the dramatic stress drop recorded in the fracture systems models (Figure 8) and the onset of nonuniversal aperture-to-length scaling, because stress amplification dominates the long fractures comprising the multiple-segment zone and stress shielding dominates the shorter fractures outside the zone.

Acknowledgments
We thank Ian Main and Carl Renshaw for providing the data shown in Figures 1a and 1b, respectively. Discussions with Ian Main on nonuniversal scaling and bilinear fitting are most appreciated. We thank Peter Cundall and Dave Potyondy for sharing their thoughts on fracture toughness in bonded particle models. This work was supported by an Itasca Education Partnership awarded to Franziska Mayrhofer in the form of a free PFC2D license. The thorough and thoughtful comments of Jon E. Olson and an anonymous reviewer and the editorial advice of Yehuda Ben-Zion are gratefully acknowledged. The data for Figures 8 and 9 are provided as a supplementary file and data guidelines can be found in the supporting information.

References

Bathurst, R. J., & Rothenburg, L. (1988). Note on a random isotropic granular material with negative Poisson's ratio. *International Journal of Engineering Science*, *26*(4), 373–383. https://doi.org/10.1016/0020-7225(88)90116-4

Bonnet, E., Bour, O., Odling, N. E., Davy, P., Main, I., Cowie, P., & Berkowitz, B. (2001). Scaling of fracture systems in geological media. *Reviews of Geophysics*, *39*(3), 347–383. https://doi.org/10.1029/1999RG000074

Bristow, J. R. (1960). Microcracks, and the static and dynamic elastic constants of annealed and heavily cold-worked metals. *British Journal of Applied Physics*, *11*(2), 81.

Cundall, P. (1988). Formulation of a three-dimensional distinct element model. Part I. A scheme to detect and represent contacts in a system composed of many polyhedral blocks. *International Journal of Rock Mechanics and Mining Sciences and Geomechanics Abstracts*, *25*(3), 107–116. https://doi.org/10.1016/0148-9062(88)92293-0

Cundall, P., & Detournay, C. (2017). Dynamic relaxation applied to continuum and discontinuum numerical models in geomechanics. In X.-T. Feng (Ed.), *Rock Mechanics and Engineering Volume 3, Analysis, Modeling & Design* (pp. 45–90). London, UK: Taylor & Francis Group.

Fleck, N. A., Deshpande, V. S., & Ashby, M. F. (2010). Micro-architectured materials: Past, present and future. *Proceedings of the Royal Society of London A: Mathematical, Physical and Engineering Sciences*, *466*(2121), 2495–2516. https://doi.org/10.1098/rspa.2010.0215

Gaspar, N. (2010). A granular material with a negative Poisson's ratio. *Mechanics of Materials*, *42*(7), 673–677. https://doi.org/10.1016/j.mechmat.2010.05.001

Germanovich, L. N., & Astakhov, D. K. (2004). Fracture closure in extension and mechanical interaction of parallel joints. *Journal of Geophysical Research*, *109*, B02208. https://doi.org/10.1029/2002JB002131

Griffiths, D., & Mustoe, G. G. (2001). Modelling of elastic continua using a grillage of structural elements based on discrete element concepts. *International Journal for Numerical Methods in Engineering*, *50*(7), 1759–1775.

Gross, D., & Seelig, T. (2011). *Fracture mechanics: With an Introduction to Micromechanics*. Berlin: Springer Science & Business Media.

Hart, R., Cundall, P., & Lemos, J. (1988). Formulation of a three-dimensional distinct element model—Part II. Mechanical calculations for motion and interaction of a system composed of many polyhedral blocks. *International Journal of Rock Mechanics and Mining Sciences and Geomechanics Abstracts*, *25*(3), 117–125. https://doi.org/10.1016/0148-9062(88)92294-2

Hatton, C. G., Main, I. G., & Meredith, P. G. (1994). Non-universal scaling of fracture length and opening displacment. *Nature*, *367*(6459), 160–162.

Hooker, J. N., & Katz, R. F. (2015). Vein spacing in extending, layered rock: The effect of synkinematic cementation. *American Journal of Science*, *315*(6), 557–588. https://doi.org/10.2475/06.2015.03

Huang, H., & Detournay, E. (2008). Intrinsic length scales in tool-rock interaction. *International Journal of Geomechanics*, *8*(1), 39–44. https://doi.org/10.1061/(ASCE)1532-3641(2008)8:1(39)

Itasca Consulting Group, Inc (2008). PFC2D (Particle Flow Code in 2 Dimensions). version 5.0. Retrieved from www.itascacg.com

Kachanov, M. (1992). Effective elastic properties of cracked solids: Critical review of some basic concepts. *Applied Mechanics Reviews*, *45*(8), 304–335. https://doi.org/10.1115/1.3119761

Kachanov, M. (2007). On the effective elastic properties of cracked solids—Editor's comments. *International Journal of Fracture*, *146*(4), 295–299. https://doi.org/10.1007/s10704-007-9170-6

Kushch, V., Sevostianov, I., & Mishnaevsky, L. (2009). Effect of crack orientation statistics on effective stiffness of mircocracked solid. *International Journal of Solids and Structures*, *46*(6), 1574–1588. https://doi.org/10.1016/j.ijsolstr.2008.11.023

Liu, C., Pollard, D. D., & Shi, B. (2013). Analytical solutions and numerical tests of elastic and failure behaviors of close-packed lattice for brittle rocks and crystals. *Journal of Geophysical Research: Solid Earth*, *118*, 71–82. https://doi.org/10.1029/2012JB009615

Main, I., Leonard, T., Papasouliotis, O., Hatton, C., & Meredith, P. (1999). One slope or two? Detecting statistically significant breaks of slope in geophysical data, with application to fracture scaling relationships. *Geophysical Research Letters*, *26*(18), 2801–2804.

Martel, S. J., & Shacat, C. (2013). Mechanics and interpretations of fault slip. In R. Abercrombie, A. McGarr, G. Di Toro, & H. Kanamori (Eds.), *Earthquakes: Radiated Energy and the Physics of Faulting*. Washington, DC: American Geophysical Union. https://doi.org/10.1029/170GM21

Mayrhofer, F., Schöpfer, M. P. J., & Grasemann, B. (2014). *Non-Universal Aperture-Length Scaling of Opening Mode Fractures, Geophysical Research Abstracts* (Vol. 16). Vienna: EGU General Assembly.

Monette, L., & Anderson, M. P. (1994). Elastic and fracture properties of the two-dimensional triangular and square lattices. *Modelling and Simulation in Materials Science and Engineering*, *2*(1), 53–66.

Olson, J. E. (1993). Joint pattern development: Effects of subcritical crack growth and mechanical crack interaction. *Journal of Geophysical Research*, *98*(B7), 12,251–12,265. https://doi.org/10.1029/93JB00779

Olson, J. E. (2003). Sublinear scaling of fracture aperture versus length: An exception or the rule? *Journal of Geophysical Research*, *108*(B9), 2413. https://doi.org/10.1029/2001JB000419

Olson, J. E. (2004). Predicting fracture swarms—The influence of subcritical crack growth and the crack-tip process on joint spacing in rock. *Geological Society London Special Publications*, *231*(1), 73–88. https://doi.org/10.1144/GSL.SP.2004.231.01.05

Olson, J., & Pollard, D. D. (1989). Inferring paleostresses from natural fracture patterns: A new method. *Geology*, *17*(4), 345. https://doi.org/10.1130/0091-7613(1989)017<0345:IPFNFP>2.3.CO;2

Olson, J. E., & Pollard, D. D. (1991). The initiation and growth of en échelon veins. *Journal of Structural Geology*, *13*(5), 595–608. https://doi.org/10.1016/0191-8141(91)90046-L

Olson, J. E., & Schultz, R. A. (2011). Comment on "A note on the scaling relations for opening mode fractures in rock" by C.H. Scholz. *Journal of Structural Geology*, *33*(10), 1523–1524. https://doi.org/10.1016/j.jsg.2011.07.004

Orlowsky, B., Saenger, E. H., Guéguen, Y., & Shapiro, S. (2003). Effects of parallel crack distributions on effective elastic properties—A numerical study. *International Journal of Fracture*, *124*(3), L171–L178. https://doi.org/10.1023/B:FRAC.0000022563.29991.80

Pollard, D. D., & Segall, P. (1987). Theoretical displacements and stresses near fractures in rock: With applications to faults, joints, veins, dikes and solution surfaces. In B. K. Atkinson (Ed.), *Fracture Mechanics of Rock* (pp. 277–349). London: Academic Press. https://doi.org/10.1016/B978-0-12-066266-1.50013-2

Pollard, D. D., Segall, P., & Delaney, P. T. (1982). Formation and interpretation of dilatant échelon cracks. *Geological Society of America Bulletin*, *93*(12), 1291–1303.

Potyondy, D. O. (2007). Simulating stress corrosion with a bonded-particle model for rock. *International Journal of Rock Mechanics and Mining Sciences*, *44*(5), 677–691. https://doi.org/10.1016/j.ijrmms.2006.10.002

Potyondy, D., & Cundall, P. (2004). A bonded-particle model for rock. *International Journal of Rock Mechanics and Mining Sciences*, *41*(8), 1329–1364. https://doi.org/10.1016/j.ijrmms.2004.09.011

Renshaw, C. E., & Park, J. C. (1997). Effect of mechanical interactions on the scaling of fracture length and aperture. *Nature*, *386*, 482–484. https://doi.org/10.1038/386482a0

Renshaw, C. E., & Pollard, D. D. (1994). Numerical simulation of fracture set formation: A fracture mechanics model consistent with experimental observations. *Journal of Geophysical Research*, *99*(B5), 9359–9372. https://doi.org/10.1029/94JB00139

Rothenburg, L., Berlin, A. A., & Bathurst, R. J. (1991). Microstructure of isotropic materials with negative Poisson's ratio. *Nature*, *354*(6353), 470–472.

Schijve, J. (1996). Some calculations on the stress distribution in an infinite sheet with a single crack and with periodic collinear cracks. *Engineering Fracture Mechanics*, *55*(2), 313–320. https://doi.org/10.1016/0013-7944(96)00048-3

Scholz, C. H. (2010). A note on the scaling relations for opening mode fractures in rock. *Journal of Structural Geology*, *32*(10), 1485–1487. https://doi.org/10.1016/j.jsg.2010.09.007

Scholz, C. H. (2011). Reply to comments of Jon Olson and Richard Schultz. *Journal of Structural Geology*, *33*(10), 1525–1526. https://doi.org/10.1016/j.jsg.2011.07.006

Schöpfer, M. P., Arslan, A., Walsh, J. J., & Childs, C. (2011). Reconciliation of contrasting theories for fracture spacing in layered rocks. *Journal of Structural Geology*, *33*(4), 551–565. https://doi.org/10.1016/j.jsg.2011.01.008

Schultz, R. A., Klimczak, C., Fossen, H., Olson, J. E., Exner, U., Reeves, D. M., & Soliva, R. (2013). Statistical tests of scaling relationships for geologic structures. *Journal of Structural Geology*, *48*, 85–94. https://doi.org/10.1016/j.jsg.2012.12.005

Schultz, R. A., Soliva, R., Fossen, H., Okubo, C. H., & Reeves, D. M. (2008). Dependence of displacementlength scaling relations for fractures and deformation bands on the volumetric changes across them. *Journal of Structural Geology*, *30*(11), 1405–1411. https://doi.org/10.1016/j.jsg.2008.08.001

Segall, P. (1984). Formation and growth of extensional fracture sets. *Geological Society of America Bulletin*, *95*(4), 454–462.

Spyropoulos, C., Scholz, C. H., & Shaw, B. E. (2002). Transition regimes for growing crack populations. *Physical Review E*, *65*(5), 056105. https://doi.org/10.1103/PhysRevE.65.056105

Tada, H., Paris, P. C., & Irwin, G. R. (2000). *The stress analysis of cracks handbook* (3rd ed.). New York: American Society of Mechanical Engineers. https://doi.org/10.1115/1.801535

Toomey, A., & Bean, C. J. (2000). Numerical simulation of seismic waves using a discrete particle scheme. *Geophysical Journal International*, *141*(3), 595–604. https://doi.org/10.1046/j.1365-246x.2000.00094.x

Vermilye, J. M., & Scholz, C. H. (1995). Relation between vein length and aperture. *Journal of Structural Geology*, *17*(3), 423–434. https://doi.org/10.1016/0191-8141(94)00058-8

Walmann, T., Malthe-Sørenssen, A., Feder, J., Jøssang, T., Meakin, P., & Hardy, H. (1996). Scaling relations for the lengths and widths of fractures. *Physical Review Letters*, *77*(27), 5393–5396.

Wang, Y., & Mora, P. (2008). Macroscopic elastic properties of regular lattices. *Journal of the Mechanics and Physics of Solids*, *56*(12), 3459–3474. https://doi.org/10.1016/j.jmps.2008.08.011